SAND2020-14084

SANDIA REPORT

SANDtbd-xxxx

Printed December 2020

Sandia National Laboratories

A Phenomenological Model for Cavitation

Adam C. Sokolow, Chad B. Hovey

Prepared by
Sandia National Laboratories
Albuquerque, New Mexico 87185
Livermore, California 94550

Issued by Sandia National Laboratories, operated for the United States Department of Energy by National Technology & Engineering Solutions of Sandia, LLC.

Available to DOE and DOE contractors from

U.S. Department of Energy
Office of Scientific and Technical Information
P.O. Box 62
Oak Ridge, TN 37831

Telephone:	(865) 576-8401
Facsimile:	(865) 576-5728
E-Mail:	reports@osti.gov
Online ordering:	http://www.osti.gov/scitech

Available to the public from

U.S. Department of Commerce
National Technical Information Service
5301 Shawnee Road
Alexandria, VA 22312

Telephone:	(800) 553-6847
Facsimile:	(703) 605-6900
E-Mail:	orders@ntis.gov
Online order:	https://classic.ntis.gov/help/order-methods

ABSTRACT

A phenomenological model of cavitation is presented, based on observations that both large relative negative pressures and large negative time derivatives of pressure are required for cavitation onset.

We simulated two cavitation experiments to generate cavitation scaling parameters for relative pressure drop and rate of pressure drop. Our results show the model, while simple, is effective at reproducing results from laboratory experiments of cavitation.

The parameters were then used in conjunction with a human surrogate computational model to predict, at any position within the head, the probability of intracranial cavitation caused by exposure to a blast event.

The results suggest that the magnitude of blast overpressure observed in field data is sufficient to cause intracranial cavitation. Our analysis indicates that the helmeted head, when compared to the unhelmeted head configuration, results in a decrease but not elimination of cavitation exposure. When density functions of cavitation probability versus cumulative brain volume are combined with an injury severity model, the results show helmet efficacy at low and moderate risk levels. However, the convergence of unhelmeted and helmeted probability density functions at high-to-excessive risk thresholds indicates the helmet offers diminishing protection at elevated exposure levels, relative to the unhelmeted baseline.

Future investigation and collaboration with neuroscience subject matter experts are needed to contextualize the current computational results. While the present work contributes specific and quantified predictions of intracranial cavitation location and severity, more research is required to apply our results to clinical settings with population-based brain injury subjects and controls. The relationship between our intracranial cavitation predictions with their anticipated clinical sequelae remains a topic in need of exploration.

ACKNOWLEDGMENT

- The authors gratefully acknowledge support from the Office of Naval Research (Dr. Timothy Bentley) under PANTHER grant N0001418IP00069.
- We thank Mr. Ryan J. Terpsma for his contributions of running some initial scoping calculations in CTH.
- We thank Mr. Douglas Dederman for his leadership with the ONR contract and management of Department 5421.

CONTENTS

LIST OF FIGURES

LIST OF TABLES

NOMENCLATURE

Abbreviation	Definition
ACH	Advanced Combat Helmet
APL	Applied Physics Laboratory
ARA	Applied Research Associates
CSF	cerebral spinal fluid
CTH	(not an acronym) the name of a shock hydrodynamic code at Sandia
DOE	Department of Energy
DOT	Department of Transportation
PMHS	post-mortem human subject
PPE	personal protective equipment
SIBL	Sandia Injury Biomechanics Laboratory
SNL	Sandia National Laboratories
SSM	Sierra Solid Mechanics
TBI	traumatic brain injury

1. INTRODUCTION

Cavitation in a fluid, such as water, is the phenomenon of vapor-containing bubble formation, caused by a rapid drop of pressure in the fluid. Conceptually, the pressure drop attempts to "pull apart" liquid water under high tension, causing the water volume to expand rapidly. The high pressure drop leads to a water phase change, from liquid to vapor, and small vapor cavities (bubbles) appear throughout the liquid.

Once formed, the vapor-filled bubbles are highly unstable, leading to a quick collapse, returning the vapor back to a liquid. While the bubbles generally have spherical symmetry, the collapse of the bubble generally is asymmetric, brought about by boundary conditions in the liquid, such as an adjacent hard surface or liquid impurity. The asymmetric collapse forms a water jet, with significant pressure elevation capable of damaging adjacent surfaces, such as the erosion seen in propellers, impellers, and pumps.

The formation and collapse of cavitation bubbles has long been implicated as a brain injury mechanism. [Gross, 1958] produced high-speed video of acceleration-induced cavitation in a water-filled test tube as a basis for a pressure gradient theory of intracranial cavitation. These compelling images are reproduced here as Figure 1-1.

[Ward et al., 1980] measured intracranial pressure as a function of head acceleration. Figure 1-2, a reproduction of Figure 7 from [Ward et al., 1980], shows peak relative pressure for frontal, parietal, occipital, and posterior fossa locations, with the latter demonstrating tensile pressure on the order of approximately -700 mmHg (-0.93 Bar = -93 kPa = -13.5 psi) at head acceleration levels between 4,000 and 6,000 m/s^2. [Ward et al., 1980] noted,

> "Brain injury severity is correlated with peak intracranial pressure. The results show that serious and fatal injuries occur when the pressures exceed 34 psi [234 kPa]."

The possibility of cavitation was theorized as a brain injury mechanism, wherein large negative pressures on the contrecoup location lead to cavitation.

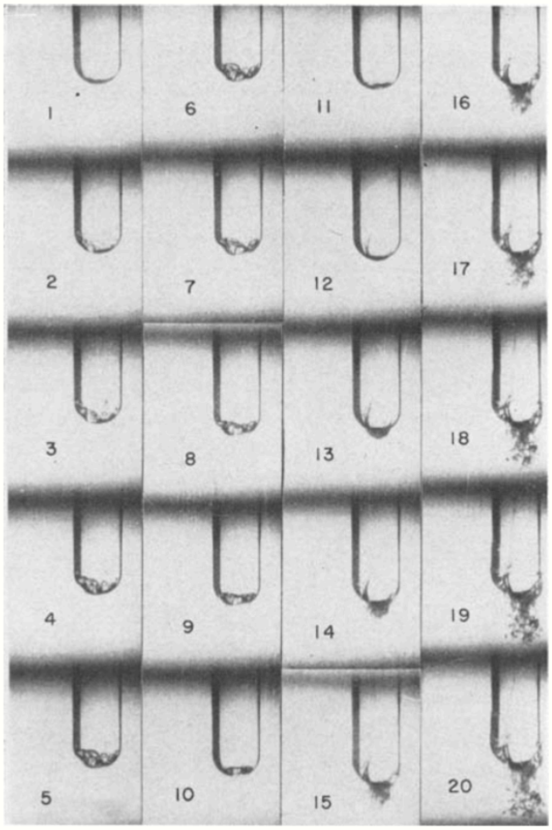

Fig. 3. High-speed photographs (4,000 frames per second) of an ordinary glass test tube, partially filled with water, being impacted from the top. Failure of tension of the fluid occurs at the base of the tube in frame 2. Final collapse of the cavity formed occurs in frame 12. The impacting force produced by the collapse of the cavity then fractures the base of the tube.

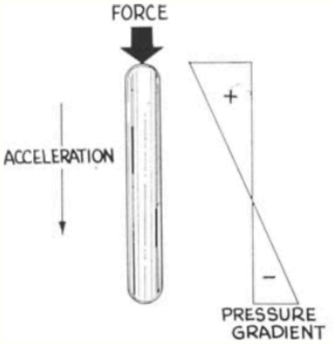

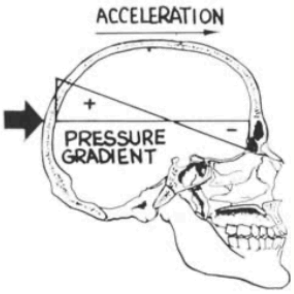

Fig. 4 (*left*). Tensile stress gradient developed in the fluid contained in a closed tube because of acceleration produced by impact to one end.

Fig. 5 (*right*). Tensile stress gradient developed in the fluid of the brain because of acceleration produced by impact.

Figure 1-1. Reproduction of [Gross, 1958] Figures 3–5, showing acceleration-induced cavitation and pressure gradient, as a basis for the intracranial cavitation theory of brain injury.

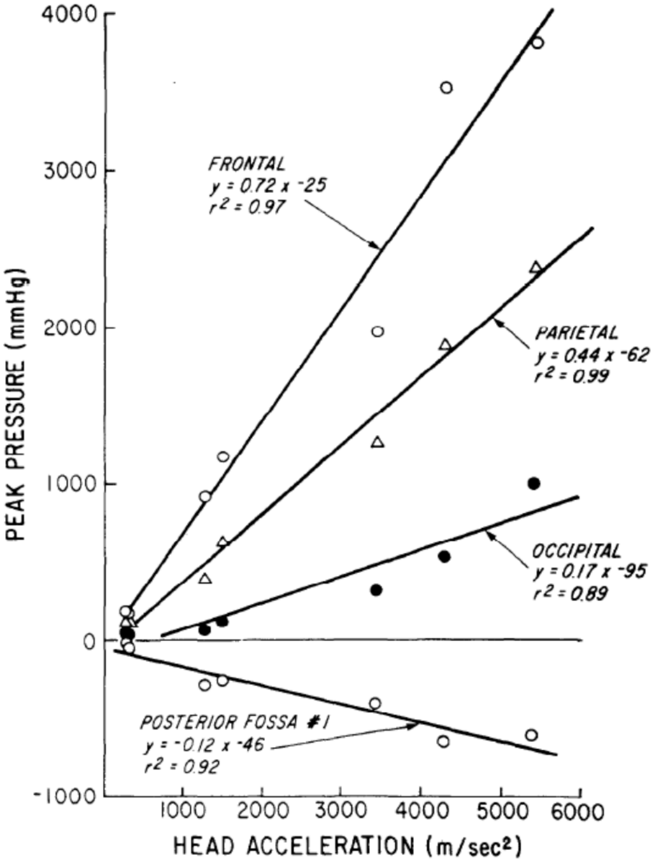

Fig. 7 - Regression analysis of peak pressure-head acceleration relationship

Figure 1-2. Reproduction of [Ward et al., 1980] Figure 7, showing peak intracranial pressure versus head acceleration.

Finally, we mention, in brief, some additional contributions that provide context to the theory of cavitation-induced brain injury:

- [Hickling and Plesset, 1964] provided numerical solutions to the equations of motion that govern collapse of a spherical bubble in water.
- [Lubock and Goldsmith, 1980] studied the impact response of two fluid-filled head and neck models, finding resulting cavitation and lending support for the cavitation theory of brain injury.
- [Chafi et al., 2009] described a 3D nonlinear finite element model to study human brain response to a shock wave at a stand-off distance of 0.8 m (2.62 feet) from 0.038, 0.093, and 0.23 kg (0.0838, 0.205, and 0.5 pounds) of TNT.
- [Salzar et al., 2017], like [Ward et al., 1980], measured intracranial pressures in post-mortem human subjects (PHMS). However, the Salzar work examined intracranial pressure gradients due to blast exposure, whereas the Ward context was an acceleration exposure.
- [Taylor and Ford, 2009] and [Taylor et al., 2014] used a high-fidelity numerical human surrogate model in conjunction the Tillotson-Brundage equation-of-state to demonstrate the potential for intracranial cavitation to occur secondary to blast exposure. From these macroscale results, [Haniff and Taylor, 2017] investigated microscale bubble collapse.
- [Gupta and Przekwas, 2013] provided a review of the current mathematical model of blast-induced traumatic brain injury.

While many existing models have sought to predict intracranial cavitation, they are often complex in their formulation, and can be prone to mesh-dependent errors caused by multi-scale effects.

We hypothesized that a simpler, phenomenological model might be sufficiently endowed to capture cavitation events without suffering undue complexity brought on by multi-scale behaviors. Moreover, to our knowledge, this is the first study that ties human head exposure of blast overpressure to injury risk through expectation of cavitation mapped to human brain anatomy.

In the following sections, we motivate the need for a simplified, phenomenological model. We then explicate the model formulation and details. Next, we apply the model to a conceptual scenario, two cavitation experiments, and a human head numerical surrogate. We then summarize and discuss the results, followed by our conclusions drawn from this modeling effort.

2. MOTIVATION

Figure 2-1 shows 10 example convergence tests using the Tillotson-Brundage cavitation model as implemented in Sierra Solid Mechanics (SSM). The model allows for tensile pressures (negative relative pressures) to exist in a material, down to a predefined cavitation pressure. Additional tensile pressures below the cavitation pressure are marked by an increase in displacement, an indicator of cavitation onset, as the presence of bubble formation increases the element size. During this expansion, the pressure remains constant; there is no resisting force since surface tension effects are absent in the model.[1]

In all simulations, the Z-domain is 10 cm long, fixed at the origin and pulled at uniform velocity at the boundary at 10 cm. In Figure 2-1, grey filled regions represent grey matter, and white regions white matter.[2] The displacements (ΔZ) are shown by the colored lines. The red color represents the test with 50 elements along the Z-axis. A progressively larger element count is thereafter used, with color coding as shown in Table 2-1.

Table 2-1. Convergence test element count parameter and color code.

	color	color code	integer map	element count
🟥	red	`rgb(255, 0, 0)`	100	50
🟩	green	`rgb( 0, 255, 0)`	010	100
🟦	cyan	`rgb( 0, 255, 255)`	011	150
🟦	blue	`rgb( 0, 0, 255)`	001	200
⬛	black	`rgb( 0, 0, 0)`	000	250

The results in Figure 2-2 show mesh dependency, a highly undesired result. While convergence toward the high-density mesh (black, 250 elements) is weakly suggested by the coarser meshes, it remains too far from ideal to be realistically considered as a viable candidate for use in simulations.

With cavitation pressure met, displacement serves as proxy for cavitation, as explained above. The coarse meshes predicts cavitation to be highly localized, at times, near the beginning or end of the domain, and at other times, near the grey-white interface. In contrast, the 250-element mesh predicts cavitation throughout the domain, with grey-white interface cavitation predicted at higher levels except for at the third case, where grey extends over [0, 5].

---

[1] The concept of reaching a critical value, beyond which, increases in displacement generate no increases in internal force is an attribute of an elastic, perfectly-plastic material laws, and thus is a conceptual analogue to the cavitation model as implemented in SSM.

[2] See report SAND2020-11444 [Terpsma and Hovey, 2020] for details on material properties.

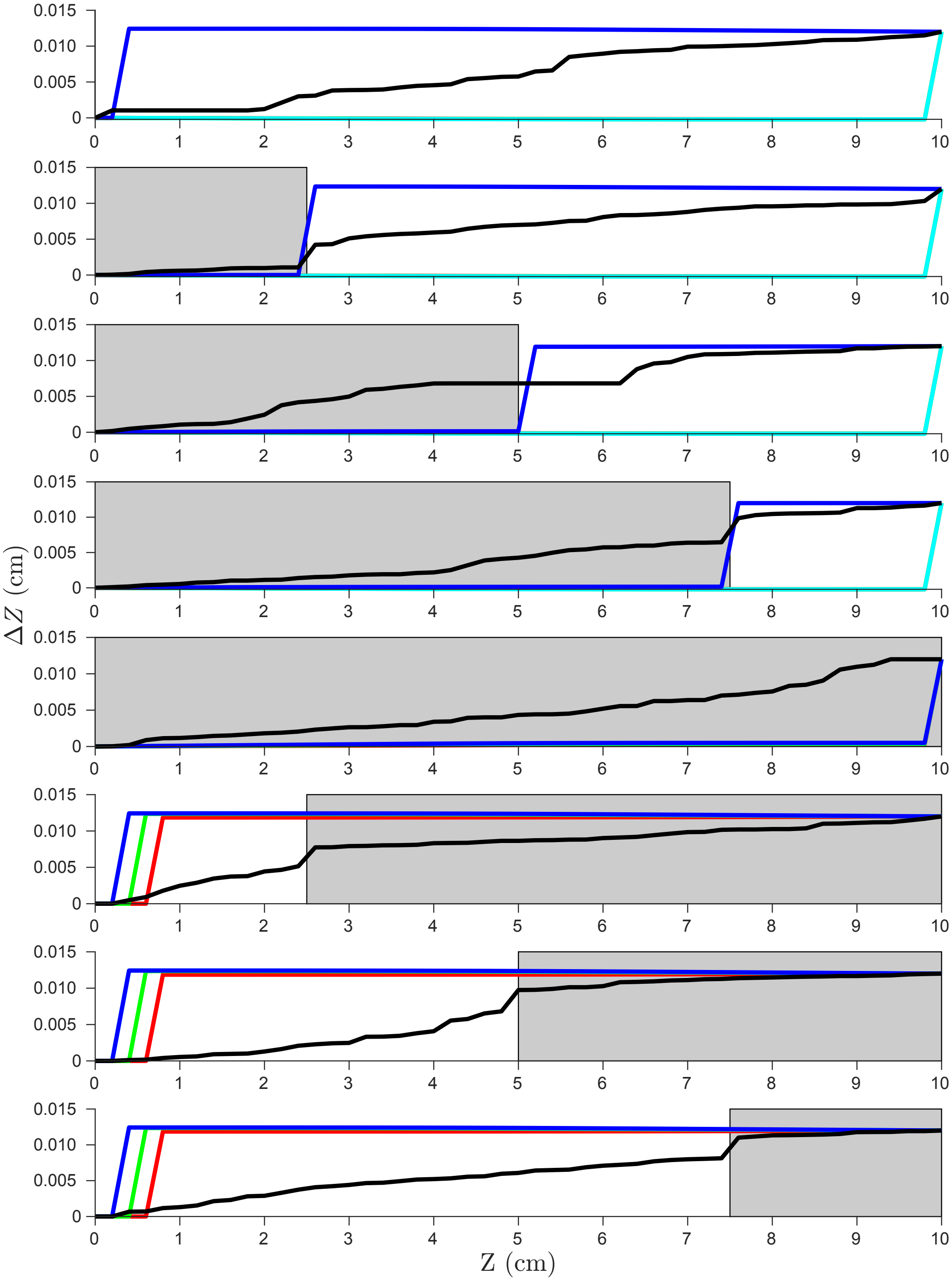

Figure 2-1. Convergence test with SSM Tillotson-Brundage model.

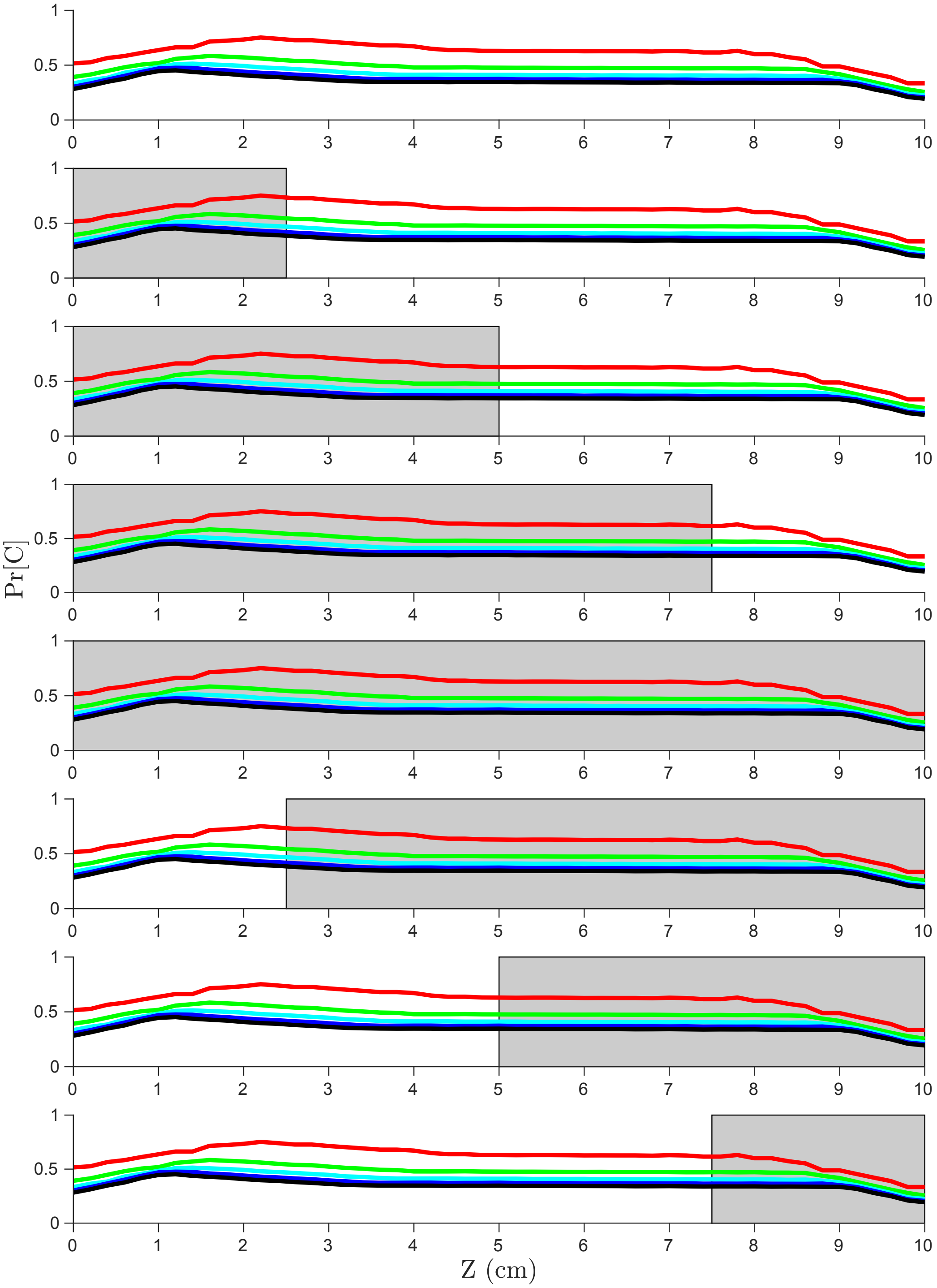

Figure 2-2. Convergence test with SSM finite deformation elastic model.

By contrast, the proposed model demonstrates convergence, shown in Fig. 2-2. Indeed, such an outcome is expected, since we have sole-substituted the Tillotson-Brundage material model with a finite deformation elastic material model. The latter model shows mesh independence, and convergence to a displacement field.

In light of these two unit tests, we began to inquire: Could cavitation prediction be adapted to a post-processing step, rather than a material modeling step, justifiable through the significant multi-scale nature of cavitation?

That is, we were concerned with bulk behavior on the centimeter scale, while seeking to track effects occurring on the micrometer scale. Would micrometer-scale displacements caused by a cloud of cavitation bubbles add to displacement, to a sufficient degree, to cause noticeable differences between the baseline case of non-cavitated bulk deformation caused by wave mechanics alone?

To propose answers to these questions, we began to develop a phenomenological model of cavitation that was sensitive to both large relative negative pressures and large negative time derivatives of pressure. In the following sections, we review the model formulation and details.

3. METHODS

3.1. Formulation

The objective of the phenomenological model is to relate a mechanical state, *i.e.*, pressure, that is favorable for a cavitation bubble to form with a probability. These probabilities vary in time due to the dynamics of the system and are integrated in time to produce the final likelihood of cavitation as a spatial variable. We denote the probability of a cavitation event C at a specific location X and time t as $\mathrm{Pr}(\mathrm{C}; X, t)$. The total likelihood of a cavitation event C occurring at some location X is then

$$\mathrm{Pr}(\mathrm{C}; X) = \min\left(1, \int_0^\infty \mathrm{Pr}[\mathrm{C}; X, t]\ \mathrm{d}t\right). \tag{3.1}$$

In the finite element model, $\mathrm{Pr}(\mathrm{C}; X)$ is a state variable that is integrated using a forward-Euler method, where the instantaneous probability $\mathrm{Pr}(\mathrm{C}; X, t)$ is determined by the criteria outlined below. Pressure $P = P(X, t) \in \mathbb{R}$ is a time and space dependent variable, with positive pressures taken as compressive and negative pressures taken as tensile. Several conditions must be met for cavitation to occur.

3.1.1. *Criterion 1: Sufficient Tensile Pressure*

To produce a non-zero probability of cavitation, the pressure P needs to be sufficiently tensile as to exceed a threshold for cavitation $\mathsf{P}_{\mathsf{cav}} \in \mathbb{R}^-$, *i.e.,*

$$\texttt{if}\ \ P < \mathsf{P}_{\mathsf{cav}} \tag{3.2}$$

$$\texttt{then}\ \ \mathrm{Pr}[\mathrm{C}; X, t] = \alpha > 0, \qquad \text{s.t. } \alpha \in \mathbb{R}^+ \text{ and } t \in [0, \infty). \tag{3.3}$$

When $P(X, t) < \mathsf{P}_{\mathsf{cav}}$, the α variable is the probability of cavitation occurring per unit time in a stable tensile state at a given location X and at a given time t. When $P < \mathsf{P}_{\mathsf{cav}}$, the accumulated probability that cavitation will occur during a time interval from t_0 to t_1 during the event time $t \in [0, \infty)$ at location X is thus

$$\mathrm{Pr}(\mathrm{C}; X) = \min\left(1, \int_{t_0}^{t_1} \alpha\ \mathrm{d}t\right) = \min\left(1, \alpha\ (t_1 - t_0)\right). \tag{3.4}$$

We see that α is then simply a constant scaling of the time interval $t \in [t_0, t_1]$ during the event time $t \in [0, \infty)$ when the pressure is sufficiently tensile, $P(X) < \mathsf{P}_{\mathsf{cav}}$.

3.1.2. *Criterion 2: Rapid Pressure Decrease*

To produce a non-zero probability of cavitation, the pressure time derivative must be rapidly decreasing. We parse “rapid decrease” as follows: A decrease in pressure from a relatively compressive to a relatively tensile state requires the time derivative be negative,

$$\texttt{and if}\ \frac{\partial P}{\partial t} < 0. \tag{3.5}$$

Several additional requirements on the derivative are made. First, the derivative must be finite,

$$\texttt{and if} - \infty < \frac{\partial P}{\partial t}. \tag{3.6}$$

Second, the derivative must be sufficiently negative to allow surface tension and inertial effects to be overcome. We denote this derivative threshold $\overset{\circ}{\mathsf{P}}_{\mathsf{cav}} \in \mathbb{R}^-$. Thus

$$\texttt{and if}\ \frac{\partial P}{\partial t} < \overset{\circ}{\mathsf{P}}_{\mathsf{cav}}. \tag{3.7}$$

With (3.7), slow pressure evolutions are disregarded. Finally, we wish to exclude noise in the pressure time derivative evolution. We enforce a high frequency cutoff $\overset{\circ}{\mathsf{P}}_{\mathsf{cut}}$ condition,

$$\texttt{and if}\ \overset{\circ}{\mathsf{P}}_{\mathsf{cut}} < \frac{\partial P}{\partial t}. \tag{3.8}$$

Conceptually, (3.8) places a high frequency cutoff on the frequency of the time derivative, omitting noise present in the underlying signal as a potential for cavitation generation. With time derivative criterion and its additional caveats in place, we now present the additive criteria.

3.1.3. *Additive Criteria*

We present the pressure and pressure time derivative criteria in an additive form,

$$\texttt{then instead}\ \Pr[\mathrm{C}; X, t] = (\alpha + \beta) > 0, \qquad \text{s.t. } \alpha, \beta \in \mathbb{R}^+ \text{ and } t \in [0, \infty). \tag{3.9}$$

The additivity allows for each parameter to contribute to the cavitation probability independent of one another. However, we should emphasize that Criterion 1 and Criterion 2 must *both* be met for non-zero cavitation probabilities to be predicted with pressure time derivatives.

Referred to as **cavitation parameters**, α and β are used to reproduce results found in cavitation experiments. When neither the α nor the β condition occurs, the probability of cavitation is zero,

$$\texttt{else}\ \Pr[\mathrm{C}; X, t] = 0. \tag{3.10}$$

When $P < \mathsf{P}_{\mathsf{cav}}$ and the pressure time derivative conditions are active, additivity allows (3.4) to be rewritten to include β as

$$\Pr(\mathrm{C}; X) = \min\left(1, \int_{t_0}^{t_1} (\alpha + \beta)\ \mathrm{d}t\right) = \min\left(1, (\alpha + \beta)\ (t_1 - t_0)\right). \tag{3.11}$$

We see that $(\alpha + \beta)$ is simply a bilinear, constant scaling of the time interval $t \in [t_0, t_1]$ during the event time $t \in [0, \infty)$ when the pressure $P(X)$ is sufficiently tensile at location X **and** the pressure time derivative conditions outlined in Criterion 2 have been met.

3.2. Conceptualization

Oftentimes, the concept of a Minimum Working Example (MWE) is used because it illustrates the mechanics of solving a software problem without any additional complexities of the actual underlying system. In this spirit, we first illustrate the cavitation model formulated in Section 3.1 with a MWE that demonstrates the accumulation of cavitation probabilities from both the tensile pressure condition and the negative pressure time derivative condition, characterized through α and β, respectively.

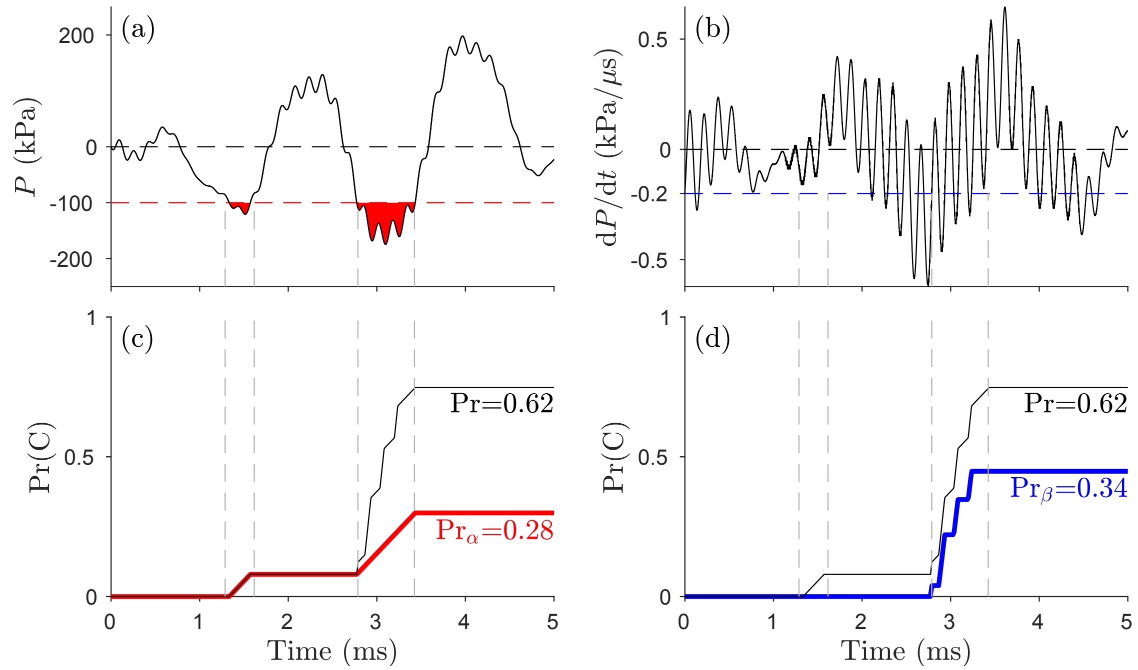

Figure 3-1. Illustration of the cavitation model through a conceptual example of a pressure time history.

Consider the conceptual example shown in Figure 3-1. The pressure time evolution at some point X is shown in Figure 3-1(a). Pressure starts at zero, then fluctuates in time between approximately 200 kPa gage (29.0 psig), highly compressive, and -200 kPa gage (-29.0 psig), highly tensile.

The threshold for cavitation, $\mathsf{P}_{\mathsf{cav}}$, is set to -100 kPa gage (-14.5 psig), indicated with the red, dashed, horizontal line. During the pressure time evolution, non-zero α contributions are accumulated when the pressure drops below the cavitation pressure threshold. These contributions in time are shown in Figure 3-1(a) with a red fill, near the 1.5 ms and 3 ms times, approximately. When $P < \mathsf{P}_{\mathsf{cav}}$ is satisfied, the probability of cavitation from α increases, shown in Figure 3-1(c). The total contribution from pressure residing below the cavitation pressure threshold to the cavitation probability during the event is 28 percent, shown in Figure 3-1(c) with a solid red piecewise linear curve.

Next, consider the pressure time derivative evolution shown in Figure 3-1(b). The pressure time derivative threshold, $\overset{\circ}{\mathsf{P}}_{\mathsf{cav}}$, is set to -0.2 kPa/$\mu$s (-2.9e-2 psi/$\mu$s), indicated with the blue, dashed, horizontal line. Dashed, vertical, gray lines in all subfigures (a)–(d) bracket the times when $P < \mathsf{P}_{\mathsf{cav}}$. Only during these times can β contribute non-zero probability of cavitation. During the first bracket, near 1.5 ms, the $P < \mathsf{P}_{\mathsf{cav}}$ condition is satisfied, but the pressure time derivative is not sufficiently negative, thus no β contribution is accumulated. During the next and final bracket when $P < \mathsf{P}_{\mathsf{cav}}$ is again satisfied, near 3 ms, the pressure time derivative becomes intermittently negative, and thus intermittently contributes to non-zero cavitation probabilities when $\mathrm{d}P/\mathrm{d}t < \overset{\circ}{\mathsf{P}}_{\mathsf{cav}}$.[1] The total contribution from pressure time derivative residing below the cavitation pressure gradient threshold to the cavitation probability during the event is 34 percent, shown in Figure 3-1(d) with a solid blue piecewise linear curve. Some observations from this example can be made:

- Non-zero probability of cavitation can occur simply by dropping the pressure P to below the cavitation pressure $\mathsf{P}_{\mathsf{cav}}$. This probability is accumulated through time with the α parameter. The purpose of this parameter is to endow the model with the ability to capture cavitation arising from pressure drops, even if they are quasi-static in nature. Since our focus will be on cavitation events arising from highly dynamic, short time interval blunt impact and blast, we anticipate that our use of α will be restricted to small numbers relative to β.

- The slope of the probability accumulation through time in non-zero red curve regions of Figure 3-1(c) is identically α. Thus the units of α can be viewed as `probability` per unit `time`.

- Non-zero probability of cavitation arising from negative pressure gradients generally occur over shorter time intervals than time intervals when the pressure P is below the cavitation pressure $\mathsf{P}_{\mathsf{cav}}$. To the degree that this generalization is true for all pressure time histories, we can say that the opportunity for cavitation arising with the β parameter is less frequent than for the α parameter. This is observed by comparison of Figure 3-1(c) with (d), wherein cavitation probability increases over two time intervals for α (the red curve) but only one time interval for β (the blue curve).

---

[1] We have dispensed with the partial derivative notation, $\partial P/\partial t$, since we have once-and-for-all fixed the location X in this example.

- The slope of the probability accumulation through time in non-zero blue curve regions of Figure 3-1(d) is identically β. Thus the units of β can be viewed as `probability` per unit `time`.
- The slope of probability accumulation through time when both the pressure and pressure gradient criteria are met is $(\alpha + \beta)$, shown in Figure 3-1(c) and (d) with the solid, black curve, leading to total probability of cavitation at X to be 62 percent at the end of the event.

Table 3-1. Simulation parameters.

parameter	value
P_{cav}	-100 kPa
α	125 /s
$\overset{\circ}{P}_{cav}$	-0.2 kPa/μs
$\overset{\circ}{P}_{cut}$	-100 kPa/μs
β	3,300 /s

3.3. Validation

For the purposes of this work, we take **validation** of a numerical model to mean a model that is capable of reproducing the cavitation onset and location observed in laboratory experiments. Our validations[2] seek to confirm that the proposed model is sufficient to predict cavitation, despite its relative simplicity.

3.3.1. The Kang Experiments

Kang and coauthors [Kang et al., 2017] demonstrated the ability to create cavitation in water-filled cuvettes subjected to drop table accelerations. At drop heights of 4 and 6 cm, absence of cavitation was observed. At 8 cm however, cavitation was observed, with nucleation occurring at the trough of the acceleration time history (just after 0.5 ms) and bubble collapse initiating near 1 ms. Figure 3-2 shows Kang's three experimental acceleration histories, in addition to the acceleration time history used for our simulation. For the 8 cm case, wherein Kang observed cavitation, responsible for the high frequency oscillations between 1 and 2 ms, we filtered the acceleration time history curve with the normalized critical frequency of Wn = 0.045.

The acceleration data was integrated once in time to produce velocity and twice in time to produce displacement cuvette time histories (Fig. 3-2). Quiescent initial conditions were

---

[2] Validation answers the question, "Are you building the correct model?" In contrast, *verification* answers the question, "Are you building the model correctly?" Code verification has been performed, but is too detailed to be explicated here.

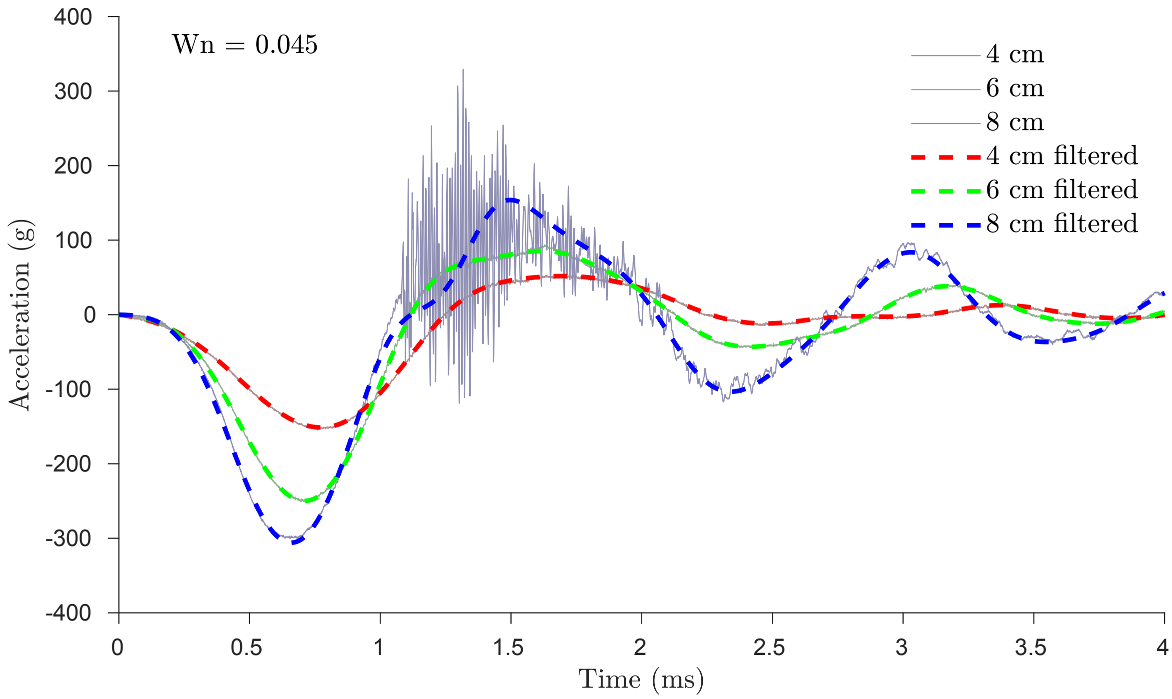

Figure 3-2. Acceleration time histories used by Kang and coauthors [Kang et al., 2017].

used. The velocity time history was used as a boundary condition for our model of Kang's experiment. Peak initial velocity exceeded 100 cm/s. Total displacement was less than 1 cm. Parameters α and β were set to values shown in Table 3-1, obtained from a parameter sweep study.

Figures 3-3 and 3-4 show, respectively, pressure and pressure time derivative as a function of time for a line of tracers located along the cuvette long axis, from top-to-bottom. Colors ranging from red, orange, yellow, green, blue, indigo were then assigned to these top-to-bottom tracers. As seen in these two figures, deviations of pressures and pressure gradients are more pronounced near the bottom of the cuvette (indigo colored); the deviations are least pronounced near the top of the cuvette (red colored). These results are consistent with Kang's experiments, indicating that only the 8 cm drop height case likely to cause cavitation, as seen in Figure 3-5.

In addition, we see the negative pressure time derivative effect, captured by the β parameter, has nearly full responsibility for causing cavitation, a result prognosticated in the observations made in Section 3.2.

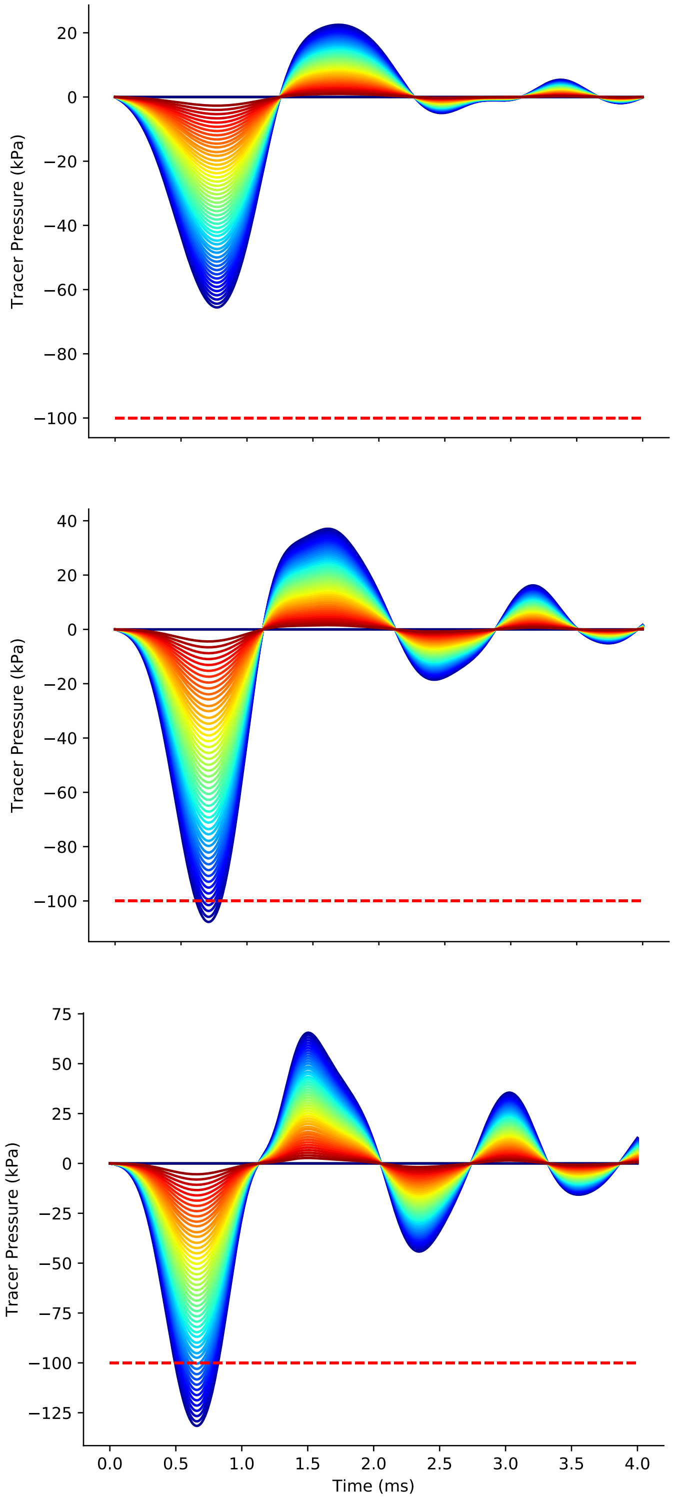

Figure 3-3. Tracer pressure as a function of time for drop heights of 4 cm (top), 6 cm (middle), and 8 cm (bottom) subfigure.

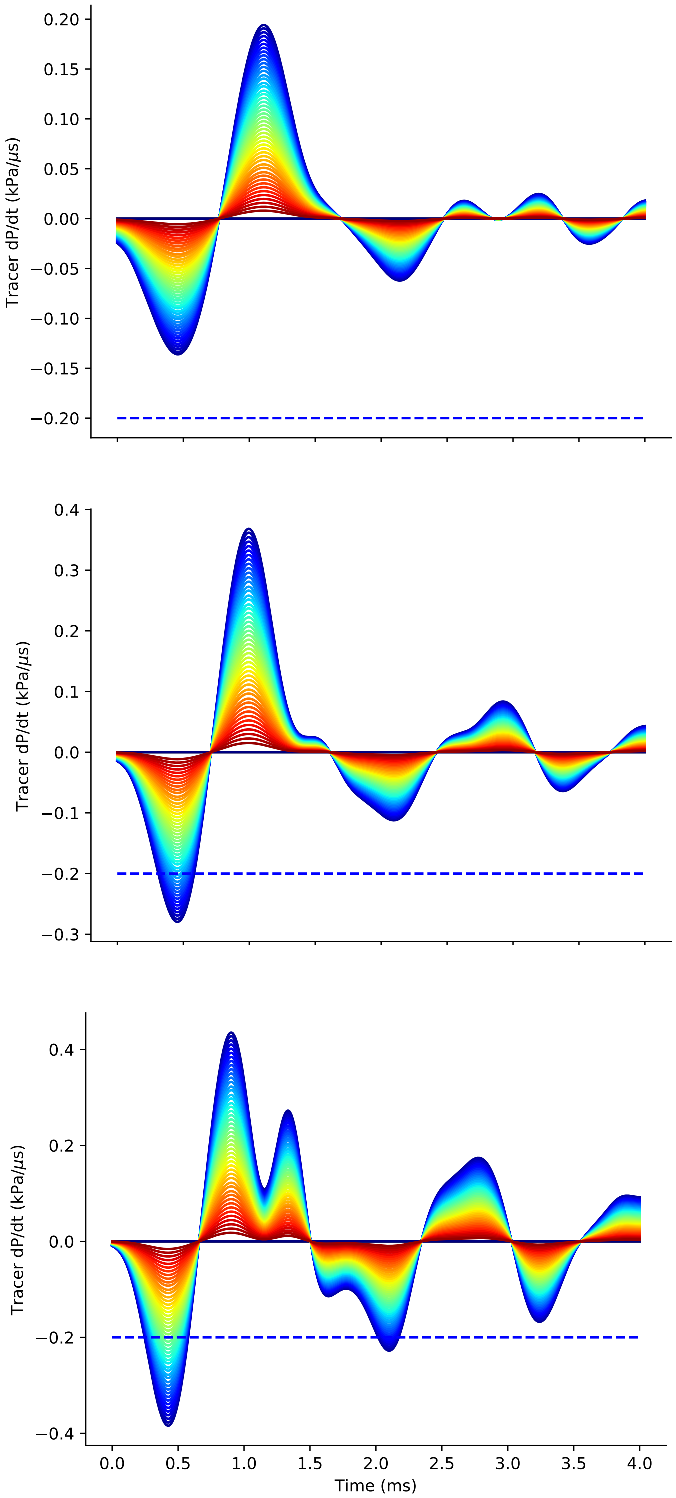

Figure 3-4. Tracer pressure gradient as a function of time for drop heights of 4 cm (top), 6 cm (middle), and 8 cm (bottom) subfigure.

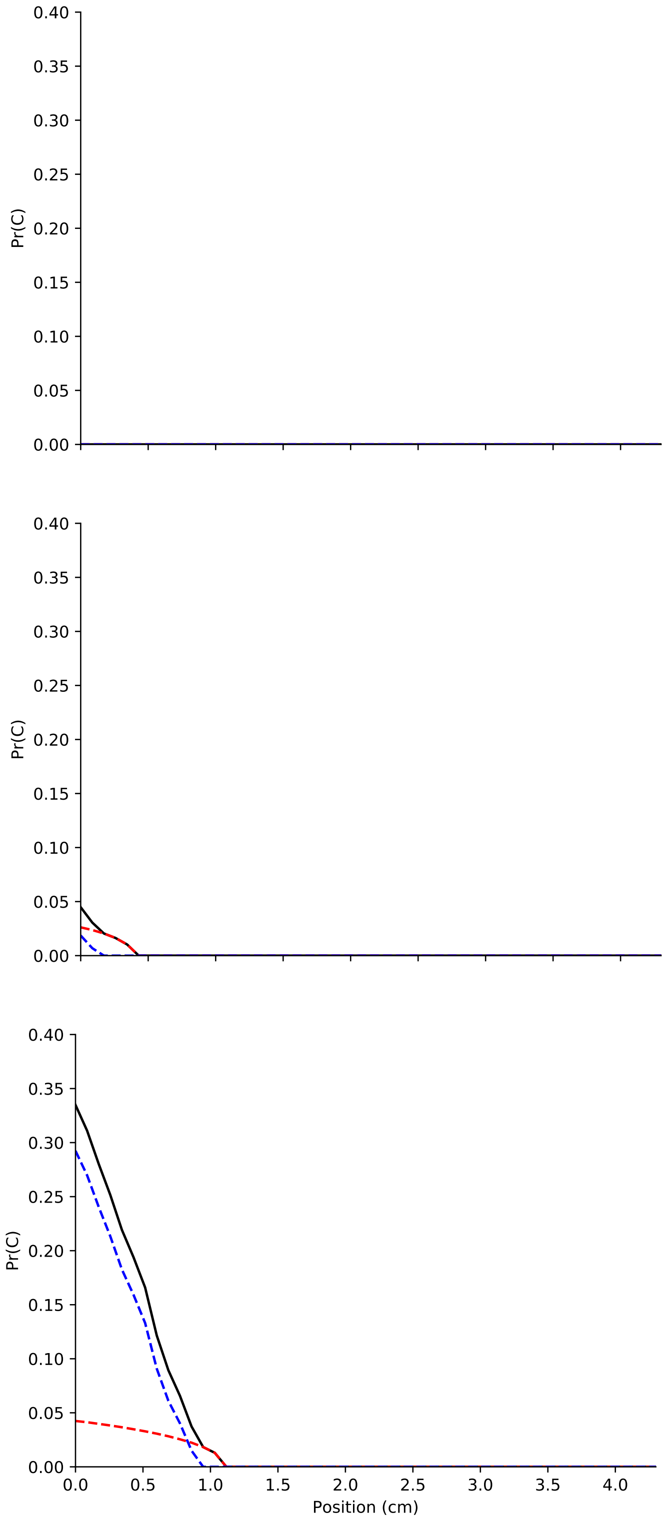

Figure 3-5. Probability of cavitation, α-effect (red, dashed), β-effect (blue, dashed), combined α and β (black, solid) as a function of scaled position along the cuvette long axis for drop heights of 4 cm (top), 6 cm (middle), and 8 cm (bottom) subfigure.

3.3.2. The Geoller Experiments

Goeller and coworkers [Goeller et al., 2012] performed shock tube experiments on a simplified human surrogate head form to demonstrate the creation of cavitation secondary to blast exposure. The ARA (Applied Research Associates) 18 inch diameter shock tube used for the experiments nominally produces overpressures on the order of 69 to 172 kPa gage (10 to 25 psig), with a pulse duration of 2 to 4 ms. Figure 3-6 shows a representative pressure time history, reproduced from Geoller's Figure 4,[3] measured at the exit of the shock tube, adjacent to the head form, with peak overpressure overpressure of 130 kPa gage (19 psig).

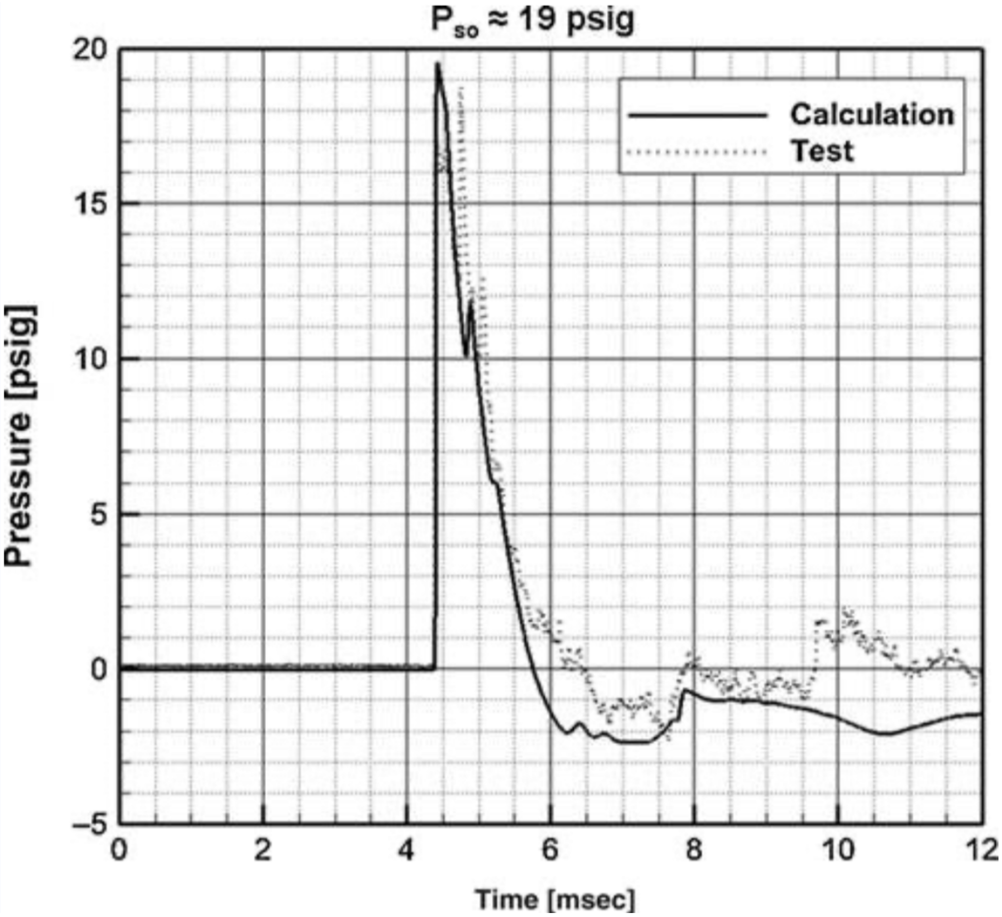

Figure 3-6. Goeller (reproduced from Fig. 4) experiment representative pressure time history.

The human surrogate head form was an ellipsoid having external dimensions of 19.2 cm in the long axis[4] and 13.7 cm in the two short axes. The ellipsoid thickness was 0.6 cm. The ellipsoid was constructed from a transparent polycarbonate-like material, Accura 60, with

---

[3] Geoller performed simulations, in addition to experiments, thus the appearance of "test" versus "calculation" in the figure.

[4] The long axis was aligned with the long axis of the shock tube.

material properties known to be elastic modulus $E = 3.0$ GPa, density $\rho = 1.21$ g/cc, and Poisson ratio $\nu = 0.22$.

Two head form fill configurations were used. The first used vacuum-degassed distilled water. The second used Sylgard gel, with bulk modulus $K = 2.19$ GPa, as a brain material surrogate, surrounded by 4 mm thick layer of degassed water.

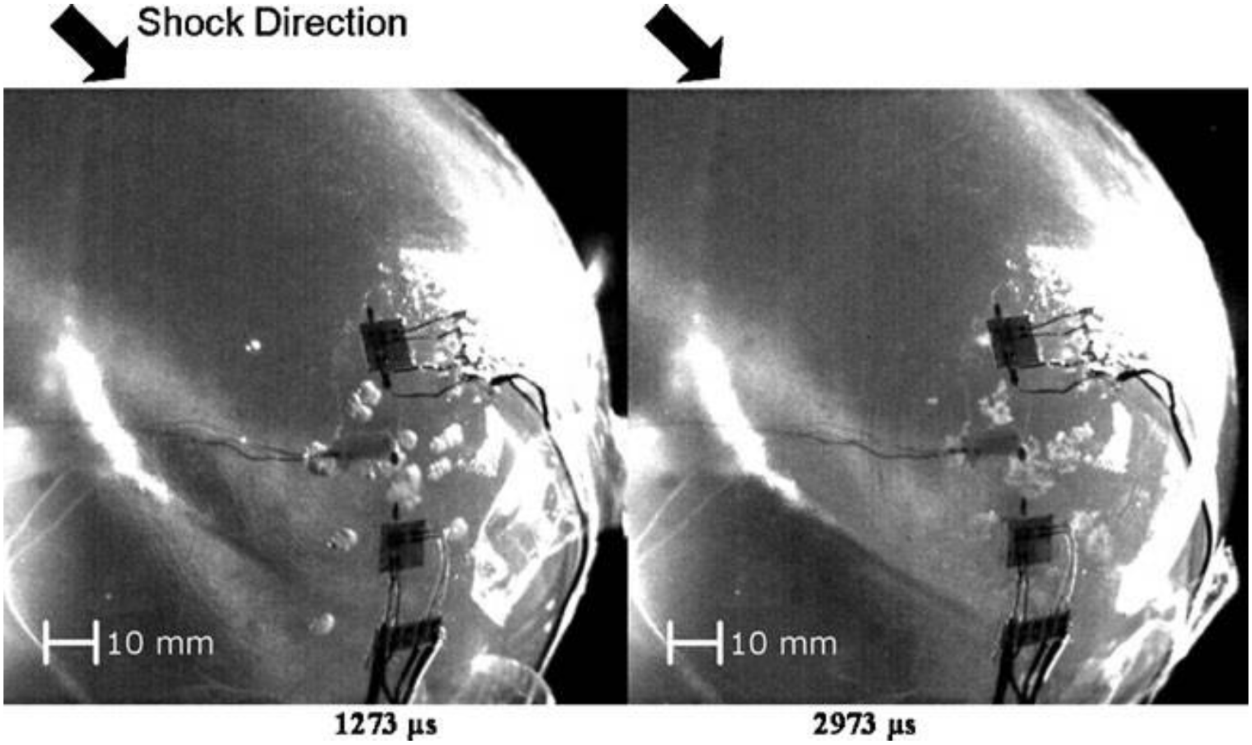

Figure 3-7. Goeller (reproduced from Fig. 10) photographs of cavitation on the countrecoup side of the head form, from test 16, first (water fill only) group, with a peak overpressure of 165 kPa gage (23.9 psig).

Geoller reported completion of 17 shock tube tests, with overpressure ranging from 51 kPa gage (7.4 psig)[5] to 165 kPa gage (23.9 psig) on the first (water only) group. They provided only two photographs of cavitation in their manuscript. These photographs are reproduced here as Figure 3-7, and show cavitation generation on the contrecoup side of the head form at 1.273 ms and 2.973 ms. The photographs are from test number 16, with 165 kPa gage (23.9 psig) overpressure.[6]

In test 16, they reported four events of cavitation creation followed by cavity collapse. The first event had bubbles of diameter from about 1 mm to 3 mm. The three subsequent cavitation events were described as "[i]ndividual bubbles were then seen to pulsate, eventually forming clusters (clouds)..." The second cavitation event, at 1.273 ms, and fourth cavitation event, at 2.973 ms are shown in Figure 3-7.

---

[5] Note this minimum is below the nominal value mentioned previously.

[6] Goeller's article did not provide a pressure time history for test 16.

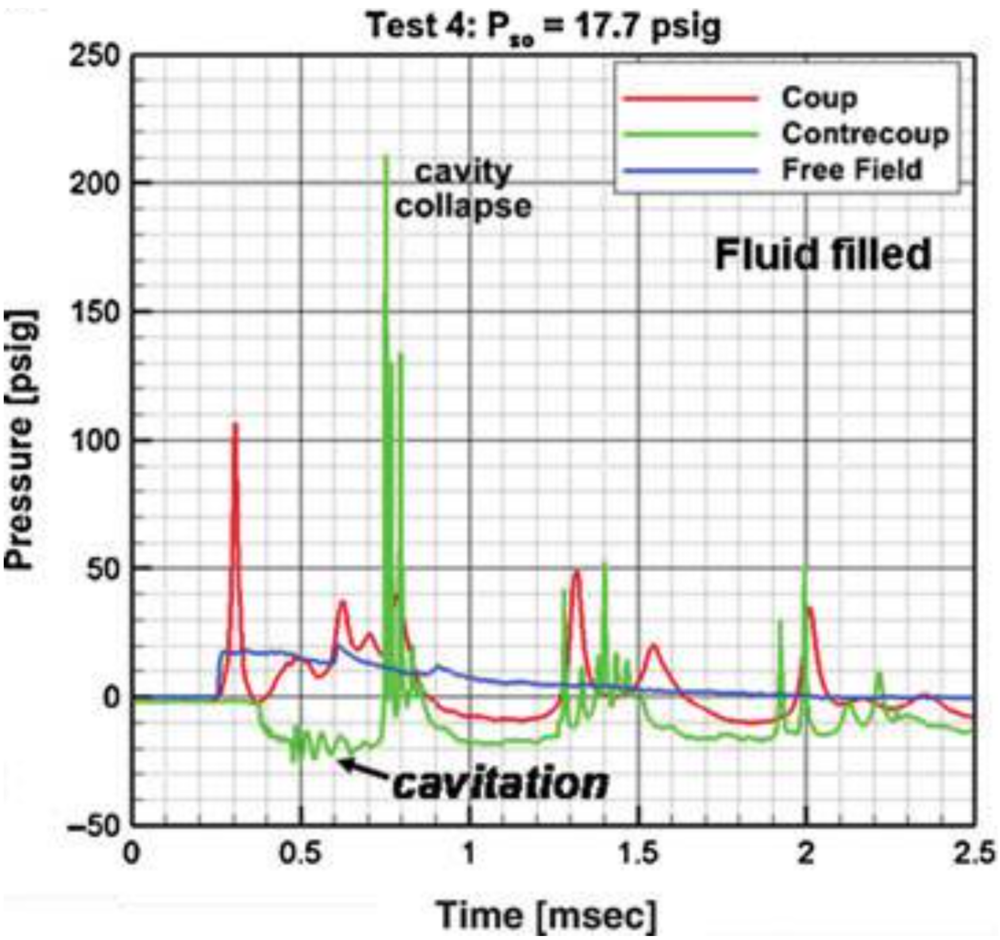

Figure 3-8. Goeller (reproduced from Fig. 8a) pressure time history for test 4 from the first (water fill only) group, with a peak over pressure of 122 kPa gage (17.7 psig).

In test 4, with a 122 kPa gage (17.7 psig) overpressure, Goeller found peak pressures at the coup location to reach approximately 689 kPa gage (100 psig), caused by the reflection of the shock wave. Figure 3-8 shows the pressure time history for this test.

They found negative pressure at the countrecoup location of approximately -117 kPa gage (-17.0 psig), creating cavitation at approximately 0.36 ms.[7] At approximately 0.80 ms, the first collapse of cavitated volume occurred, generating peak pressures of 1,450 kPa gage (210 psig).

It is interesting to note the pressure amplification:

- The 122 kPa gage blast overpressure led to peak coup overpressure of 689 kPa gage, a 5.6× increase.

---

[7] The experimental test site in Denver has an atmospheric pressure of 86.2 kPa absolute (12.5 psia), so the absolute pressure for cavitation was found to be -31 kPa absolute (-4.5 psia).

- The 122 kPa gage blast overpressure led to a peak countrecoup overpressure from cavitation cavity collapse of 1,450 kPa gage, a 11.9× increase.

We performed an initial scoping simulation of the Goeller experiments with CTH, with details shown in Figure 3-9. Figure 3-10 shows the free field incident wave used for the CTH simulation, and later for the SSM simulations applied to the Sandia head/neck human digital twin.[8] Cavitation model parameters (Table 3-1) remained the same for all simulations reported herein.

Computational results shown in Figure 3-11 compare well with qualitative experimental results reported in [Goeller et al., 2012].[9] The computational results clearly show the *coup* and *countrecoup* cavitation location demonstrated experimentally in [Goeller et al., 2012].

With results from comparison with the Kang and Geoller experiments showing promise, we next performed the extrapolatory step of applying the same blast conditions as used above in our CTH scoping simulation to the Sandia head/neck digital twin model, as an investigation of the potential for intracranial cavitation to occur, secondary to blast exposure.

---

[8] See [Terpsma and Hovey, 2020] for details.

[9] Full specimen quantitative results were not reported, though exemplar bubble diameters were reported.

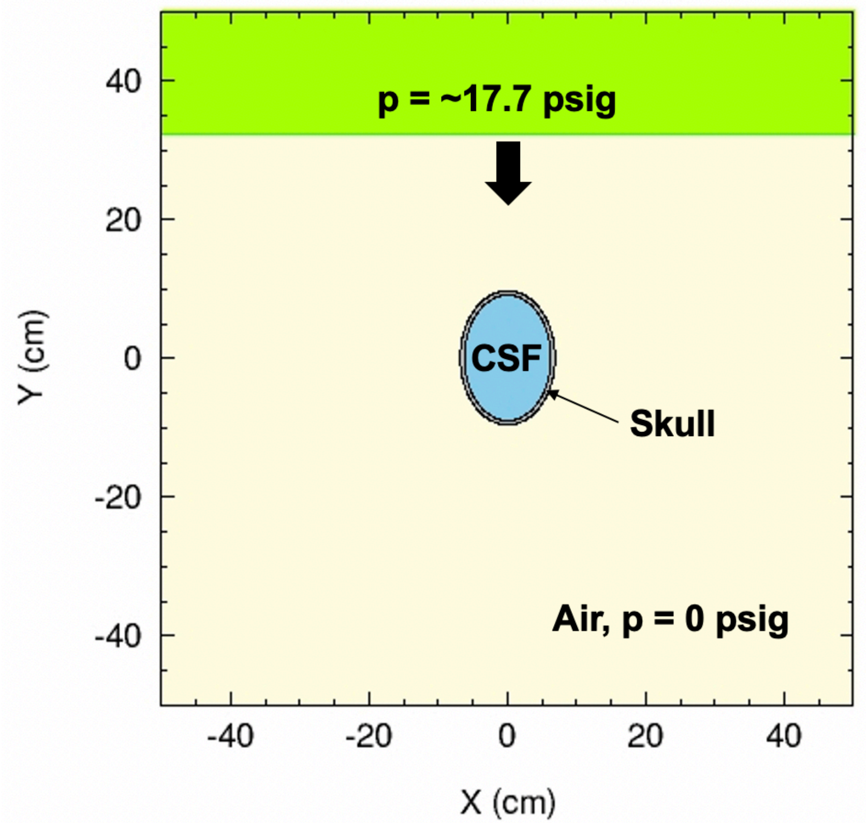

Figure 3-9. Simulation design of Goeller experiment, showing pressurized air at 122 kPa absolute (17.7 psig) approaching the Goeller ellipsoid, which is surrounded with ambient air at zero kPa absolute (0 psig).

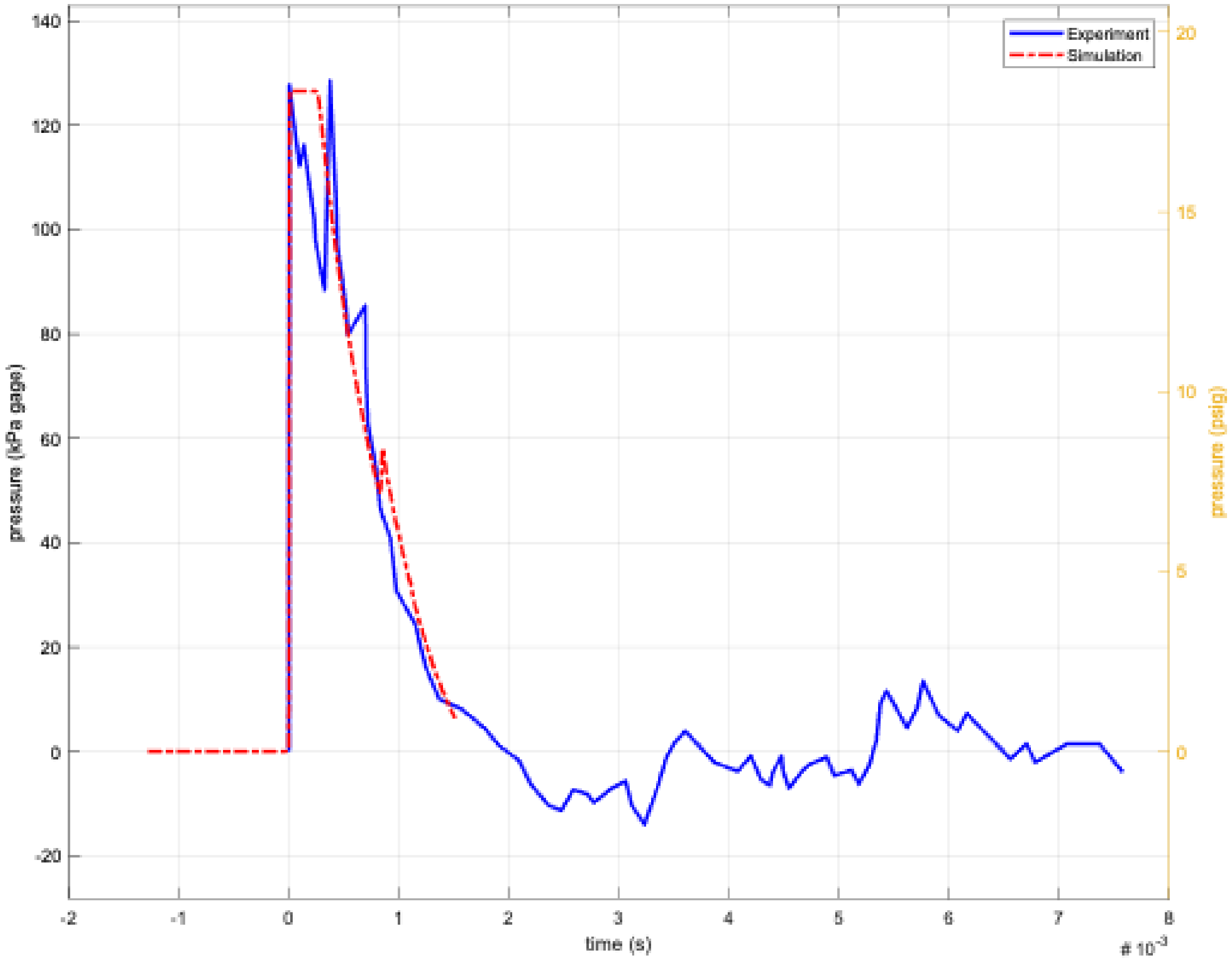

Figure 3-10. Free field incident wave applied in the Goeller experiment and applied to the digital twin simulation.

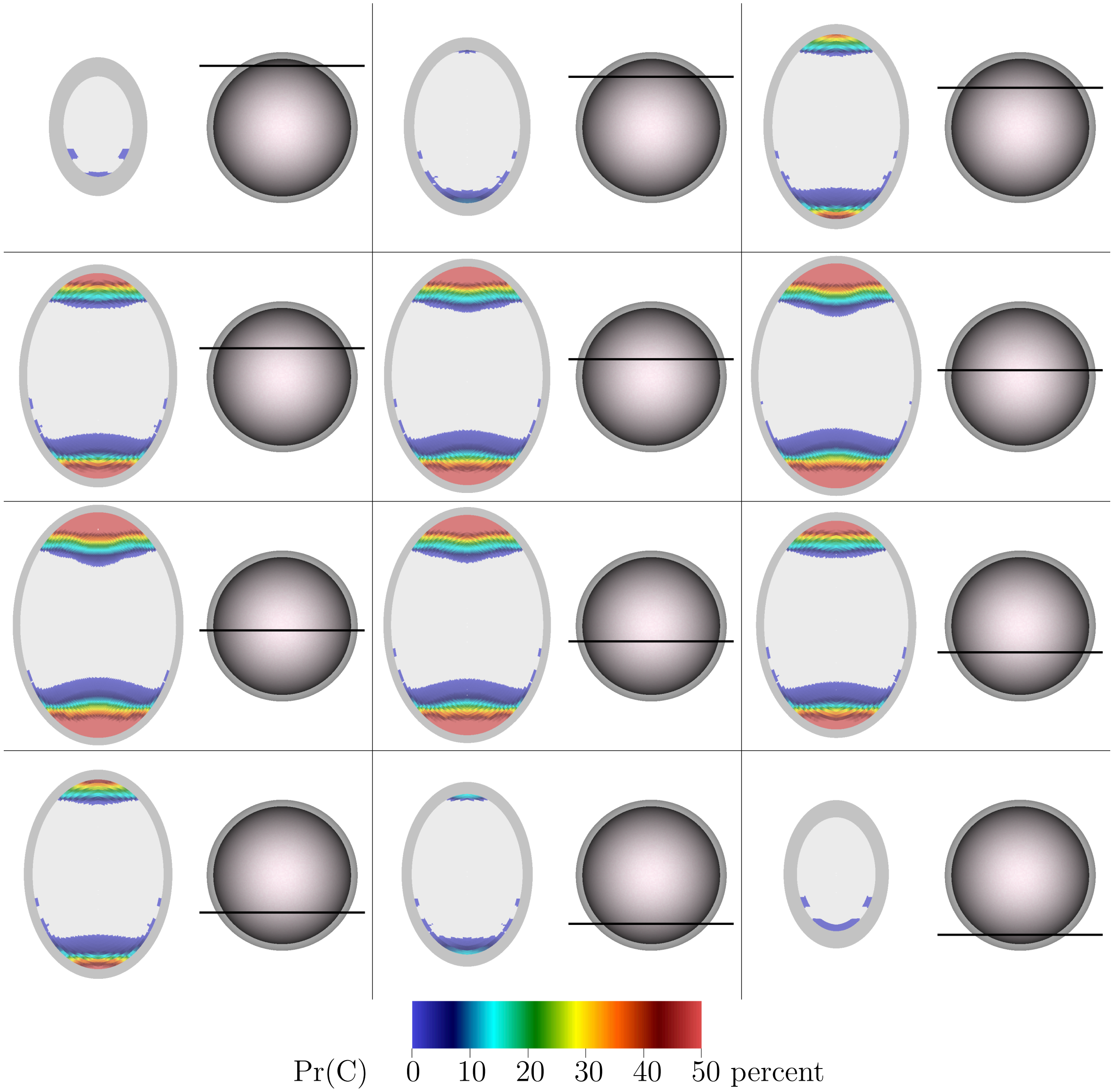

Figure 3-11. Probability of cavitation in Geoller blast scenario.

4. RESULTS

With the formulation and methods validation complete, we applied our model to the head/neck portion of the Sandia human digital twin [Terpsma and Hovey, 2020], composed of material models known to reproduce the response of human tissue. We retained the same blast exposure and same simulation model parameters used in modeling of the Goeller experiments. Thus, what resulted was a simulation where the Geoller headform was sole substituted for Sandia digital twin, all else being equal.

Two human head configurations, helmeted and unhelmeted, we considered. For convenience of comparison between these two configurations in Figure 4-1, we have presented herein the unhelmeted results to the model's right side, and the helmeted results on the model's left side, separated at the midsagittal plane and subject to the following considerations pertaining to symmetry:

- While the human twin model was not perfectly symmetric,[1] minor differences in asymmetry were not found to cause material differences left-versus-right between the helmeted and unhelmeted configurations.
- The helmet was perfectly symmetric since its fully 3D finite element mesh was constructed by reflecting a lateral half-space in the midsagittal plane.

Thus, while separate helmeted and unhelmeted simulations were undertaken, we have shown the results together in Figure 4-1 to promote comparison of the two outcomes. In each subfigure, the central image showing a frontal view of the human model, half unhelmeted and half helmeted, is for illustration purposes alone. All simulations were either fully helmeted or fully unhelmeted. Thus, the half-helmet presentation in Figure 4-1 is to assist the reader in comparison of the unhelmeted versus helmeted results; it should not be interpreted as a single simulation configuration.

Results in Figure 4-1 indicate that the helmet provides a protective mechanism against risk of cavitation exposure relative to the unhelmeted baseline. Figures 4-3 to 4-6 and Tables 4-1 to 4-2 quantify brain (white and gray matter) probability of cavitation on a per-voxel basis, with the tabulation further segregating the brain into risk exposure levels. Figure 4-7 summarizes these results in an injury risk curve.

---

[1] Humans generally have left-versus-right symmetry, but not perfectly so.

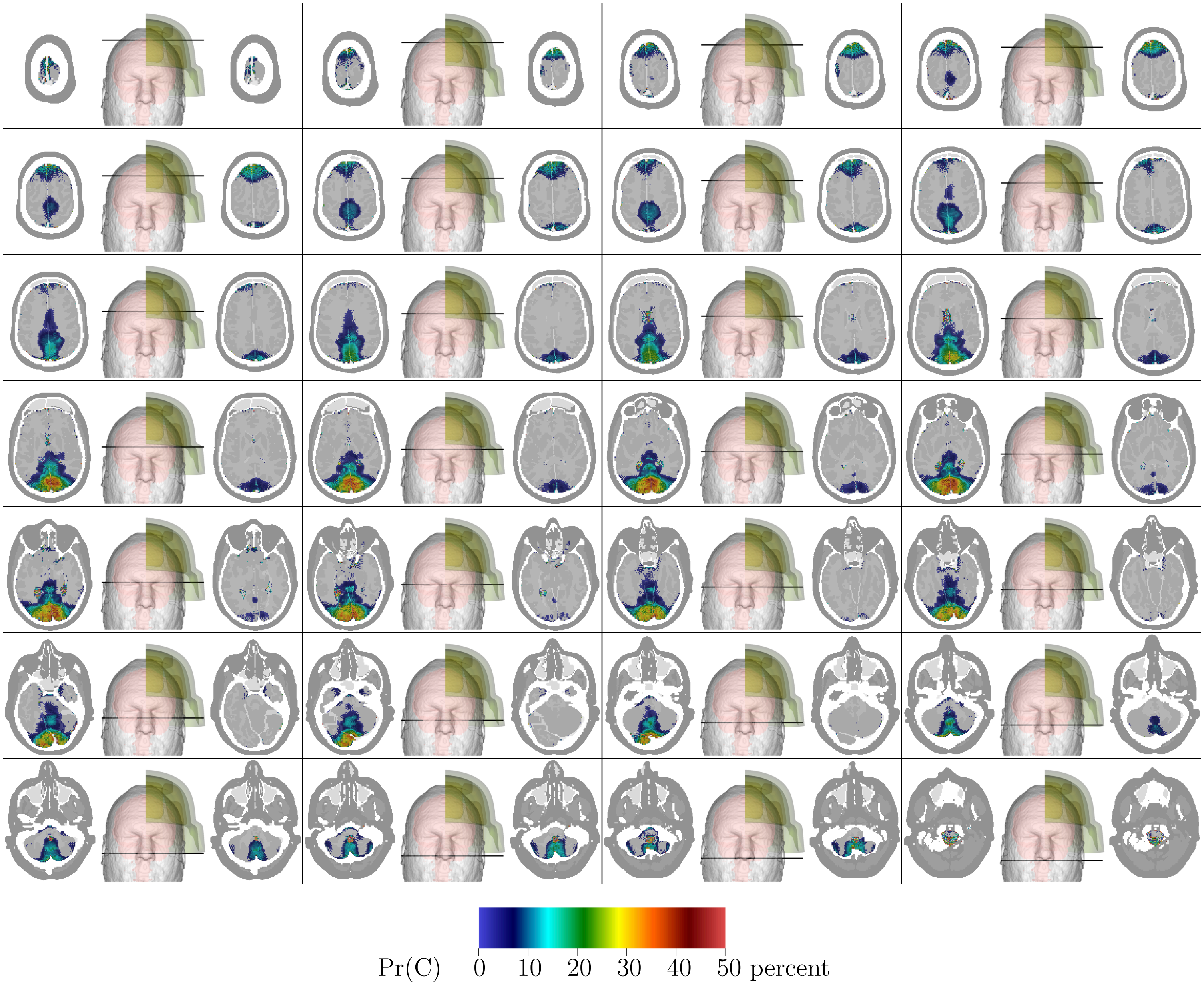

Figure 4-1. Probability of cavitation in unhelmeted and helmeted scenarios, stacked axial views.

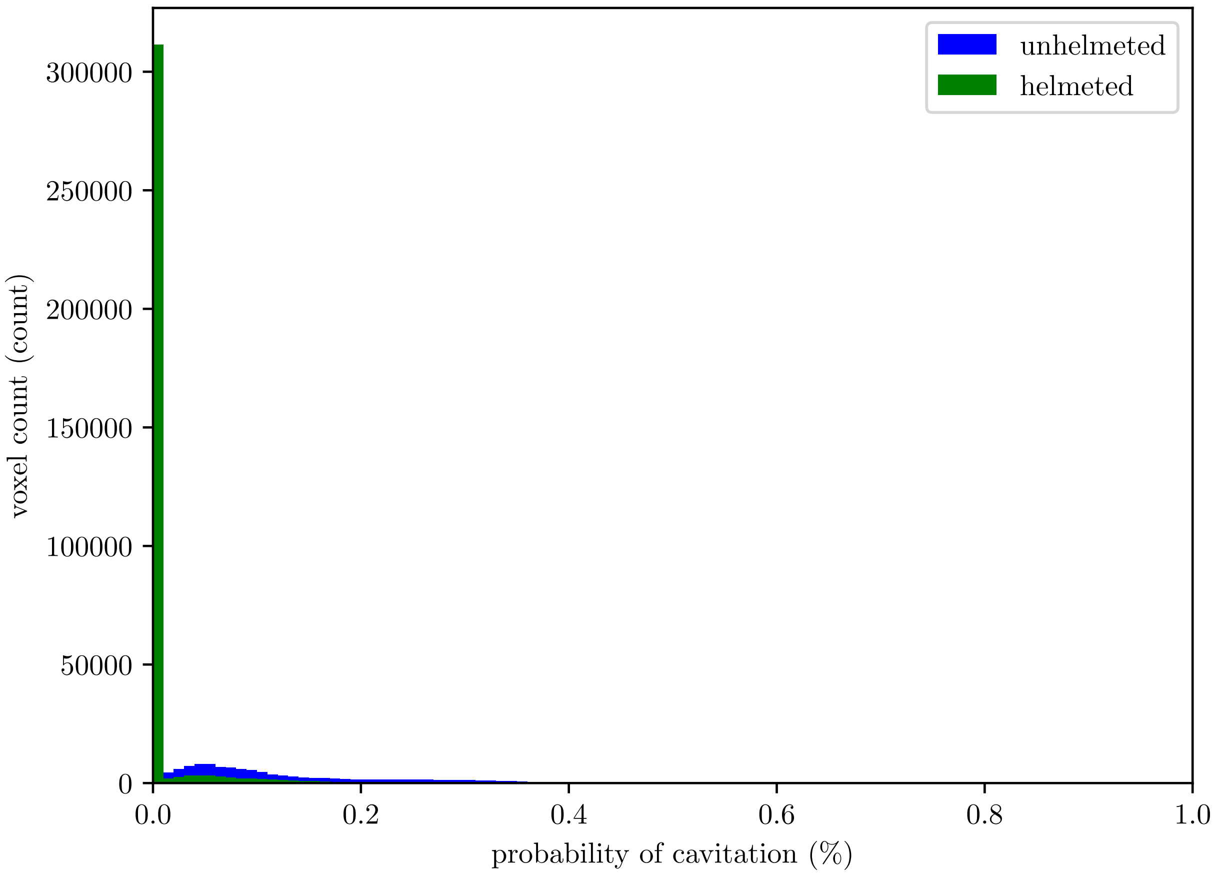

Figure 4-2. Probability of cavitation in unhelmeted and helmeted scenarios, voxel count view.

Note that Figure 4-2 reflects voxels in the brain consisting of either white matter or gray matter only. In Fig. 4-2 at zero percent probability, voxel count for helmeted exceeded nonhelmeted, indicating a protective baseline gained from helmet use. To the right (positive) of the zero percent level, unhelmeted voxel exceeded helmeted, indicating that the helmet offers some protection against cavitation, in general, across all cavitation probabilities. A zoomed-in view of the non-zero population is shown in Figure 4-3, which truncates the y-axis.

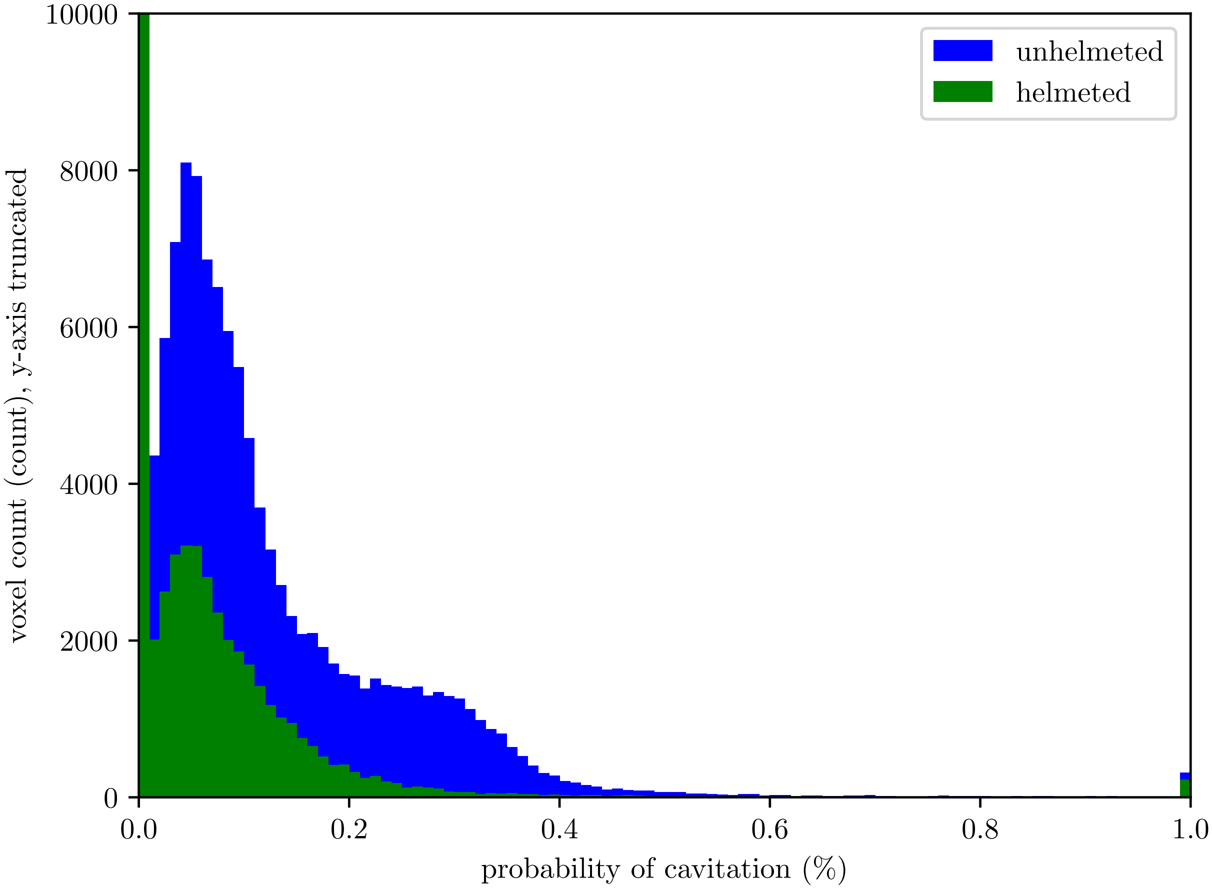

Figure 4-3. Probability of cavitation in unhelmeted and helmeted scenarios, voxel count view with y-axis truncated.

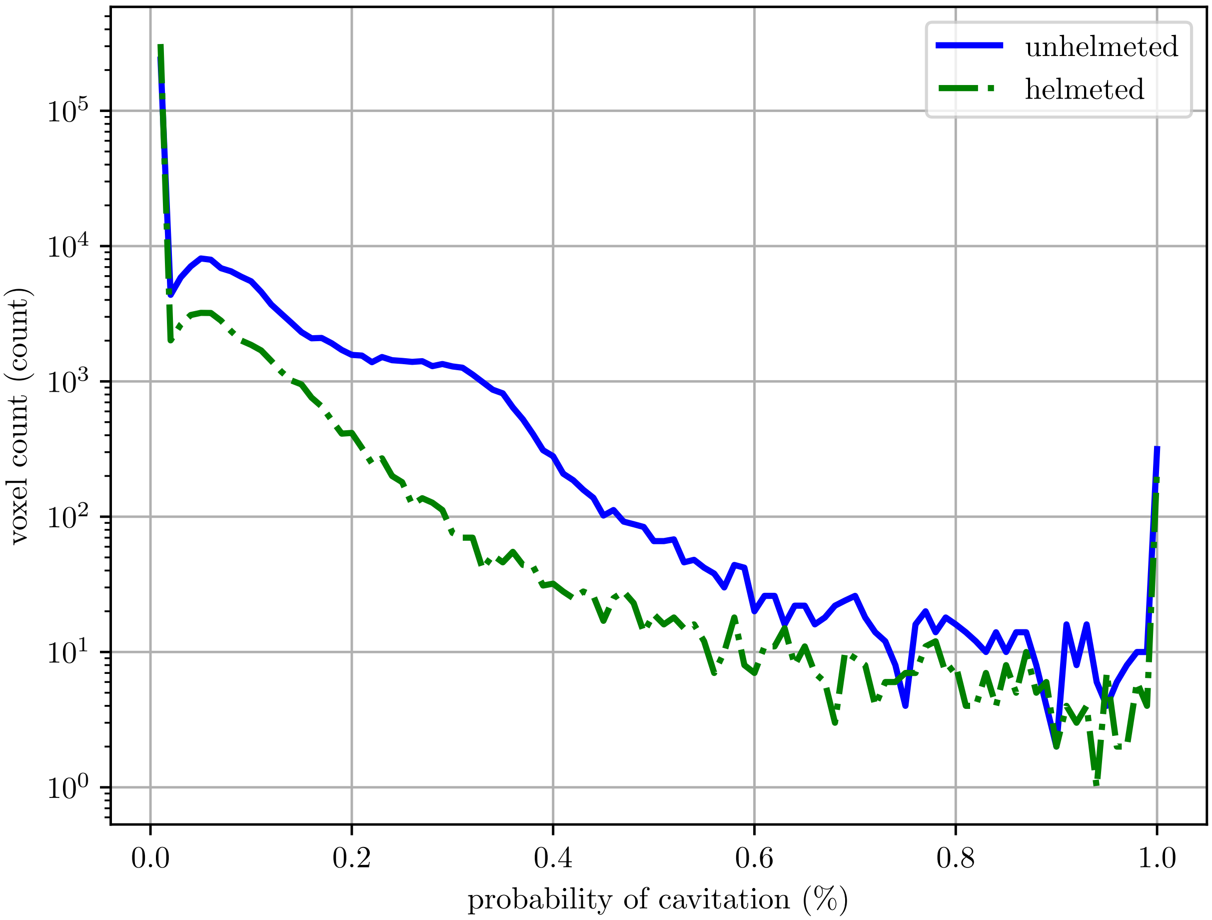

Figure 4-4. Probability of cavitation in unhelmeted and helmeted scenarios, voxel count view with logarithmic y-axis.

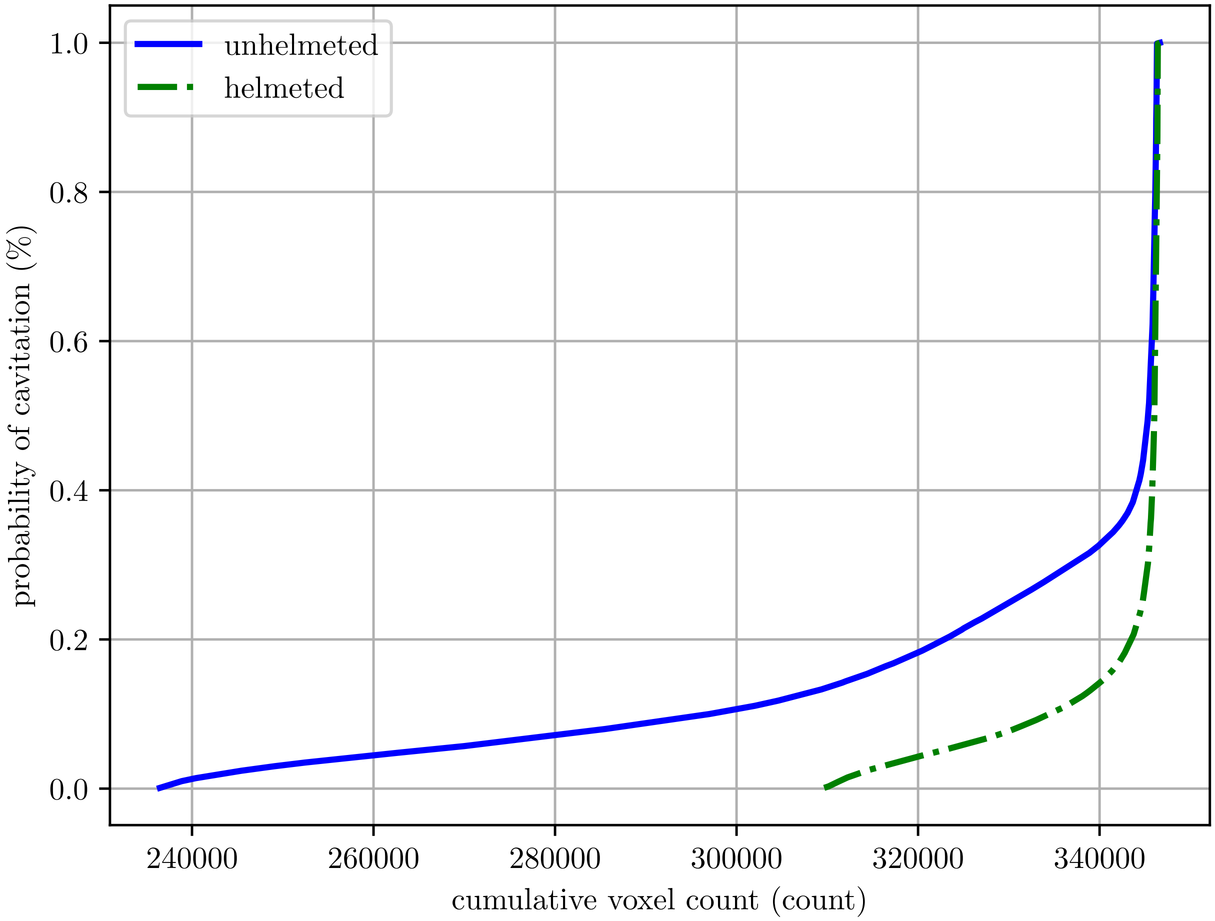

Figure 4-5. Probability of cavitation in unhelmeted and helmeted scenarios, cumulative voxel count representation.

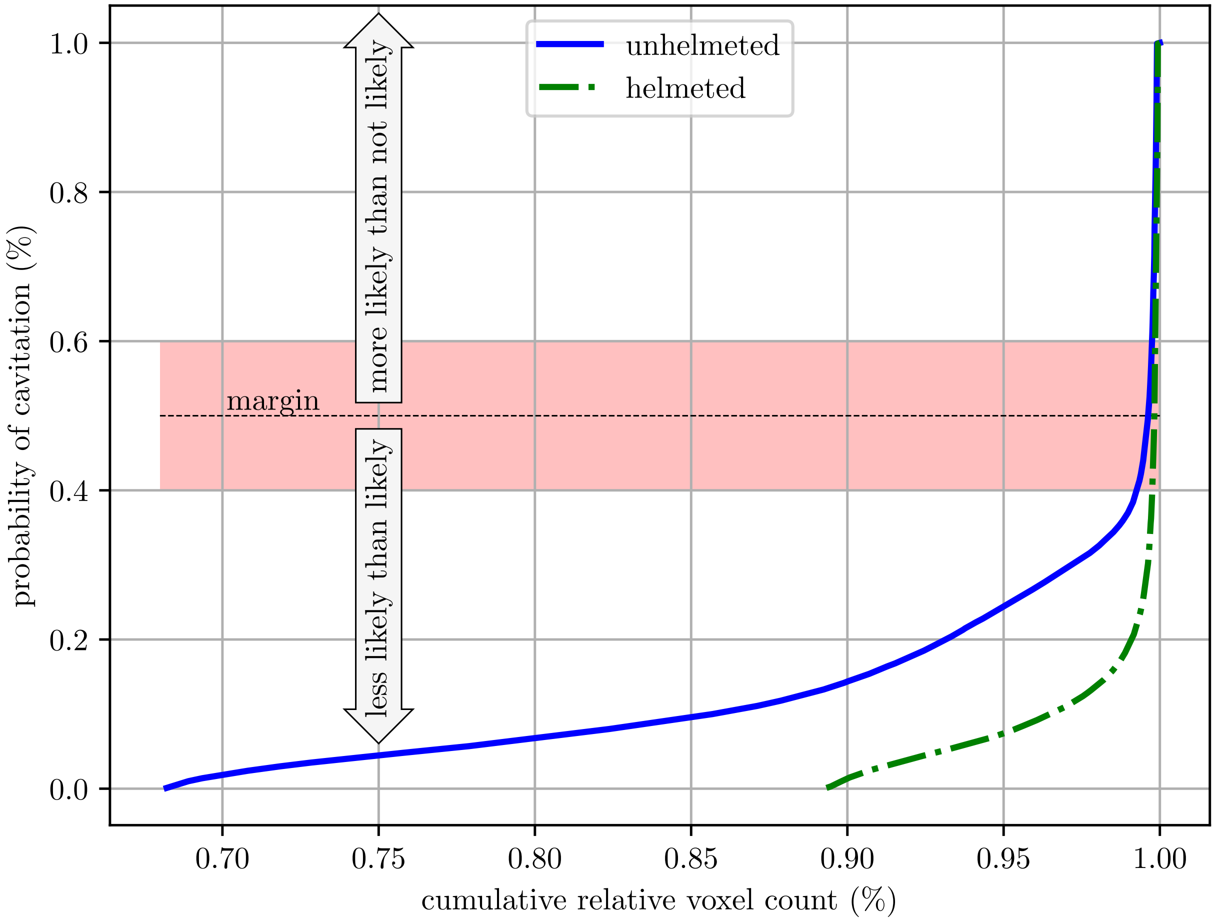

Figure 4-6. Probability of cavitation in unhelmeted and helmeted scenarios, cumulative voxel count representation, with more likely and less like divisions at the margin.

Table 4-1. Cavitation probability by coarse aggregation, three-interval ($<$ marginal, marginal, $>$ marginal), of brain volume by voxel and percent for unhelmeted and helmeted cases. Total brain volume is 346,642 voxels = 346,642 mm^3 = 0.346642 L.

		unhelmeted		helmeted	
description	Pr(C) (%)	(voxels)	(%)	(voxels)	(%)
submarginal	(0, 40]	344,104	99.268	345,799	99.757
marginal	(40, 60]	1,678	0.484	360	0.104
supramarginal	(60, 100]	860	0.248	483	0.139
	sum	346,642	100.000	346,642	100.000

Table 4-2. Cavitation probability by fine aggregation, five-interval (low, moderate, serious, high, and excessive risk), of brain volume by voxel and percent for unhelmeted and helmeted cases.

		unhelmeted		helmeted	
description	Pr(C) (%)	(voxels)	(%)	(voxels)	(%)
low risk	(0, 1]	238,864	68.908	311,329	89.813
moderate risk	(1, 10]	58,146	16.774	23,176	6.686
serious risk	(10, 40]	47,094	13.586	11,294	3.258
high risk	(40, 60]	1,678	0.484	360	0.104
excessive risk	(60, 100]	860	0.248	483	0.139
	sum	346,642	100.000	346,642	100.000

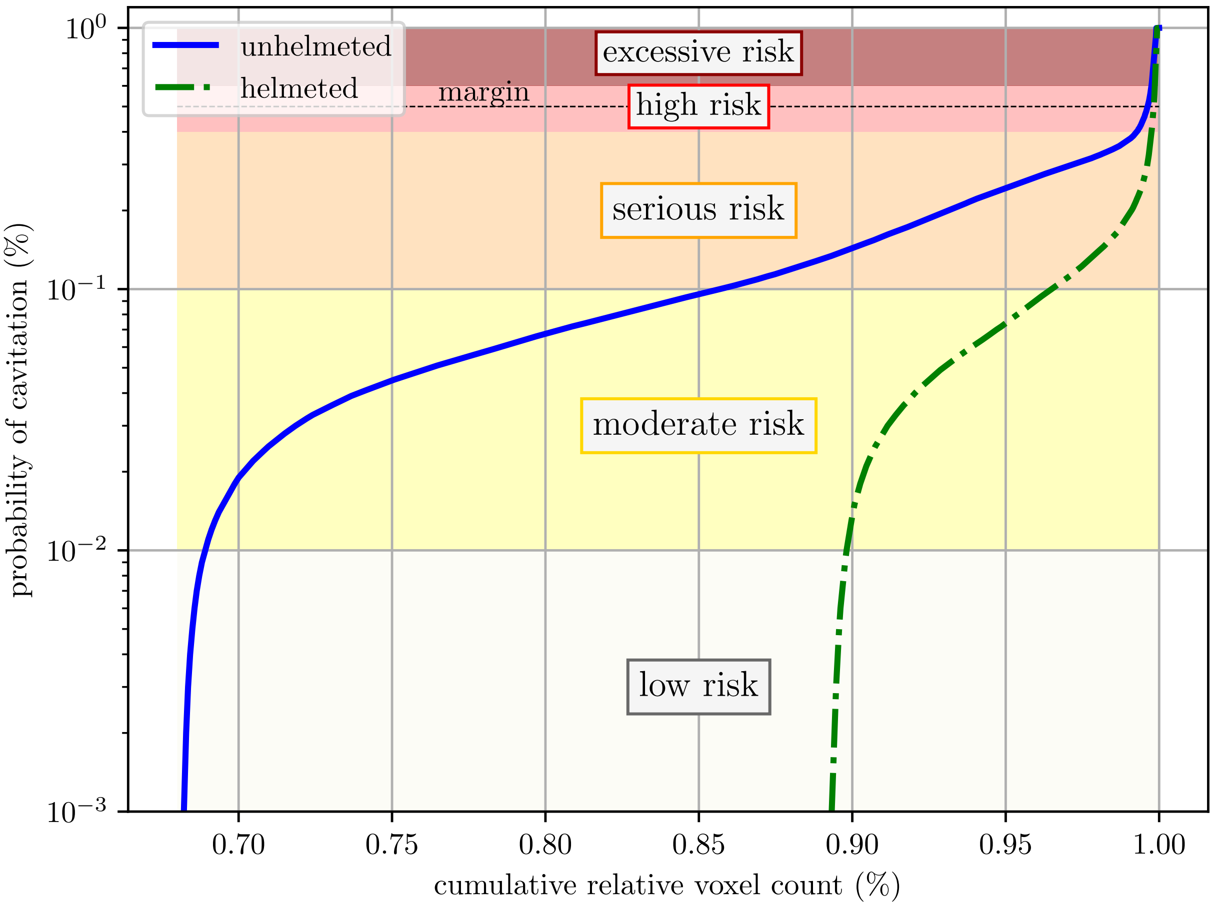

Figure 4-7. Probability of cavitation by fine aggregation risk category.

5. CONCLUSIONS

The scope of this work was limited to a pilot study to investigate the possible merits of a phenomenological model as an alternative to more complex models of cavitation.

The phenomenological model of cavitation, as presented, was based on observations that both large relative negative pressures and large negative time derivatives of pressure are required for cavitation onset.

We simulated two cavitation experiments to generate cavitation scaling parameters for relative pressure drop and rate of pressure drop. Our results showed that the model, while simple, was effective at reproducing results from laboratory experiments of cavitation.

The parameters were then used in conjunction with a human surrogate computational model to predict, at any position within the head, the probability of intracranial cavitation caused by exposure to a blast event.

The results suggest that the magnitude of blast overpressure observed in field data is sufficient to cause intracranial cavitation. Our analysis indicates that the helmeted head, when compared to the unhelmeted head configuration, results in a decrease but not elimination of cavitation exposure. When density functions of cavitation probability versus cumulative brain volume are combined with an injury severity model, the results show helmet efficacy at low and moderate risk levels. However, the convergence of unhelmeted and helmeted probability density functions at high-to-excessive risk thresholds indicates the helmet offers diminishing protection at elevated exposure levels, relative to the unhelmeted baseline.

Future investigation and collaboration with neuroscience subject matter experts are needed to contextualize the current computational results. While the present work contributes specific and quantified predictions of intracranial cavitation location and severity, more research is required to apply our results to clinical settings with population-based brain injury subjects and controls. The relationship between our intracranial cavitation predictions with their anticipated clinical sequelae remains a topic in need of exploration.

REFERENCES

[Chafi et al., 2009] Chafi, M., Karami, G., and Ziejewski, M. (2009). Computation of blast-induced traumatic brain injury. In *Summer Bioengineering Conference*, volume 48913, pages 949–950. American Society of Mechanical Engineers.

[Goeller et al., 2012] Goeller, J., Wardlaw, A., Treichler, D., O'Bruba, J., and Weiss, G. (2012). Investigation of cavitation as a possible damage mechanism in blast-induced traumatic brain injury. *Journal of Neurotrauma*, 29(10):1970–1981.

[Gross, 1958] Gross, A. G. (1958). A new theory on the dynamics of brain concussion and brain injury. *Journal of Neurosurgery*, 15(5):548–561.

[Gupta and Przekwas, 2013] Gupta, R. K. and Przekwas, A. (2013). Mathematical models of blast-induced tbi: current status, challenges, and prospects. *Frontiers in Neurology*, 4:59. `https://www.frontiersin.org/articles/10.3389/fneur.2013.00059/full`.

[Haniff and Taylor, 2017] Haniff, S. and Taylor, P. A. (2017). In silico investigation of blast-induced intracranial fluid cavitation as it potentially leads to traumatic brain injury. *Shock Waves*, 27(6):929–945. `https://www.osti.gov/pages/servlets/purl/1421630`.

[Hickling and Plesset, 1964] Hickling, R. and Plesset, M. S. (1964). Collapse and rebound of a spherical bubble in water. *The Physics of Fluids*, 7(1):7–14.

[Kang et al., 2017] Kang, W., Chen, Y., Bagchi, A., and O'Shaughnessy, T. J. (2017). Characterization and detection of acceleration-induced cavitation in soft materials using a drop-tower-based integrated system. *Review of Scientific Instruments*, 88(12):125113. `https://aip.scitation.org/doi/abs/10.1063/1.5000512`.

[Lubock and Goldsmith, 1980] Lubock, P. and Goldsmith, W. (1980). Experimental cavitation studies in a model head-neck system. *Journal of Biomechanics*, 13(12):1041–1052.

[Salzar et al., 2017] Salzar, R. S., Treichler, D., Wardlaw, A., Weiss, G., and Goeller, J. (2017). Experimental investigation of cavitation as a possible damage mechanism in blast-induced traumatic brain injury in post-mortem human subject heads. *Journal of Neurotrauma*, 34(8):1589–1602.

[Taylor and Ford, 2009] Taylor, P. A. and Ford, C. C. (2009). Simulation of blast-induced early-time intracranial wave physics leading to traumatic brain injury. *Journal of Biomechanical Engineering*, 131(6). `https://www.sandia.gov/biomechanics/_assets/documents/Taylor_2009_001.pdf`.

[Taylor et al., 2014] Taylor, P. A., Ludwigsen, J. S., and Ford, C. C. (2014). Investigation of blast-induced traumatic brain injury. *Brain Injury*, 28(7):879–895. https://doi.org/10.3109/02699052.2014.888478.

[Terpsma and Hovey, 2020] Terpsma, R. J. and Hovey, C. B. (2020). Blunt impact brain injury using cellular injury criterion. Technical report, Sandia National Lab.(SNL-NM), Albuquerque, NM (United States). https://www.sandia.gov/biomechanics/_assets/documents/Terpsma_2020_SAND2020_11444.pdf.

[Ward et al., 1980] Ward, C., Chan, M., and Nahum, A. (1980). Intracranial pressure—a brain injury criteria. In *Proceedings 24th Stapp Car Crash Conference*, volume SAE 801304, pages 3867–3880. JSTOR.

DISTRIBUTION

Email—External

Name	Company Email Address	Company Name
Timothy Bentley	timothy.b.bentley@navy.mil	Office of Naval Research US
YungChia Chen	yungchia.chen@nrl.navy.mil	Office of Naval Research US
Wonmo Kang	wonmo.kang@asu.edu	Arizona State University US
Patricia VanPoole	patricia.m.vanpoole.ctr@navy.mil	Office of Naval Research US

Email—Internal

Name	Org.	Sandia Email Address
John Niederhaus	1443	jhniede@sandia.gov
Michael Burns	5000	mjburns@sandia.gov
Dennis Helmich	5400	drhelmi@sandia.gov
Daniel Kelly	5400	dpkelly@sandia.gov
Gary Polansky	5400	gfpolan@sandia.gov
Alex Roesler	5420	awroesl@sandia.gov
Scott Miller	1542	stmille@sandia.gov
Kendall Pierson	1542	khpiers@sandia.gov
Kyran Mish	1555	kdmish@sandia.gov
Jason Brown	5421	jbrown2@sandia.gov
Candice Cooper	5421	cfcoope@sandia.gov
Douglas Dederman	5421	dadeder@sandia.gov
William Engleman	5421	wrengle@sandia.gov
Joshua Hogancamp	5421	jhoganc@sandia.gov
Chad Hovey	5421	chovey@sandia.gov
Carter Sanford	5421	cssanfo@sandia.gov
Adam Sokolow	5421	acsoko@sandia.gov
Jonathan Christensen	5422	jbchris@sandia.gov
Jeremy Laflin	5422	jlaflin@sandia.gov

Name	Org.	Sandia Email Address
Scott McEntire	5440	rmcenti@sandia.gov
Technical Library	01177	libref@sandia.gov